Atmospheric
Chemistry
and Physics
Discussions

1 # Measurement report: Molecular composition, optical

2 # properties, and radiative effects of water-soluble organic

3 # carbon in snowpack samples from Northern Xinjiang, China

4

5 Yue Zhou,[1,2] Christopher P. West,[2] Anusha P. S. Hettiyadura,[2] Xiaoying Niu,[1] Hui Wen,[1] Jiecan
6 Cui,[1] Tenglong Shi,[1] Wei Pu,[1] Xin Wang,[1,4]* Alexander Laskin[2,3]*

7

8

9 [1] *Key Laboratory for Semi-Arid Climate Change of the Ministry of Education, College of*
10 *Atmospheric Sciences, Lanzhou University, Lanzhou 730000, China*

11 [2] *Department of Chemistry,* [3] *Department of Earth Atmospheric and Planetary Sciences, Purdue*
12 *University, West Lafayette, Indiana 47906, United States*

13 [4] *Institute of Surface-Earth System Science, Tianjin University, Tianjin 300072, China*
14

15

16 *Correspondence to*: Alexander Laskin (alaskin@purdue.edu) and Xin Wang (wxin@lzu.edu.cn)

17
18
19
20
21
22
23
24
25
26
27

28   **Abstract.** Water-soluble organic carbon (WSOC) in the cryosphere has important impact on

29   the biogeochemistry cycling and snow/ice surface energy balance through changes in the

30   surface albedo. This work reports on chemical characterization of WSOC in 28 representative

31   snowpack samples collected across regional area of northern Xinjiang, northwestern China.

32   We employed multi-modal analytical chemistry techniques to investigate both bulk and

33   molecular-level composition of WSOC and its optical properties, informing the follow-up

34   radiative forcing (*RF*) modeling estimates. Based on the geographic differences and proximity

35   of emission sources, the snowpack collection sites were grouped as urban/industrial (U),

36   rural/remote (R), and soil-influenced (S) sites, for which average WSOC total mass loadings

37   were measured as 1968 ± 953 ng g^{-1} (U), 885 ± 328 ng g^{-1} (R), and 2082 ± 1438 ng g^{-1} (S),

38   respectively. The S sites showed the higher mass absorption coefficients at 365 nm (MAC_{365})

39   of 0.94 ± 0.31 m^2 g^{-1} compared to those of U and R sites (0.39 ± 0.11 m^2 g^{-1} and 0.38 ± 0.12 m^2 g^{-1}

40   $^{-1}$, respectively). Bulk composition of WSOC in the snowpack samples and its basic source

41   apportionment was inferred from the Excitation-Emission Matrices and the Parallel Factor

42   analysis featuring relative contributions of two humic-like (HULIS-1 and HULIS-2) and one

43   protein-like (PRLIS) components with ratios specific to each of the S, U, and R sites.

44   Additionally, a sample from site 120 showed unique pollutant concentrations and spectroscopic

45   features remarkably different from all other U, R, and S samples. Molecular-level

46   characterization of WSOC using high-resolution mass spectrometry (HRMS) provided further

47   insights into chemical differences among four types of samples (U, R, S, and 120). Specifically,

48   much more reduced S-containing species with high degree of unsaturation and aromaticity

49   were uniquely identified in U samples, suggesting an anthropogenic source. Aliphatic/proteins-

Atmospheric
Chemistry
and Physics
Discussions

50   like species showed highest contribution in R samples, indicating their biogenic origin. The

51   WSOC components from S samples showed high oxygenation and saturation levels. A few of

52   unique CHON and CHONS compounds with high molecular weight were detected in the 120

53   sample, which might be anthraquinone derivatives from plant debris. Modeling of the WSOC-

54   induced RF values showed warming effects of 0.04 to 0.59 W m^{-2} among different groups of

55   sites, which contribute up to 16% of that caused by BC, demonstrating the important influences

56   of WSOC on the snow energy budget.

57

1   Introduction

As the largest component of the terrestrial cryosphere (Brutel-Vuilmet et al., 2013), snow covers up to 40% of Earth's land seasonally (Hall et al., 1995). Snowfall is a crucial fresh water, nutrient, and carbon source for land ecosystems (Jones, 1999;Mladenov et al., 2012), especially for barren regions such as the northwestern China (Xu et al., 2010). Chemical deposits in the snowpack are highly photochemically and biologically active, which in turn influence biogeochemical cycles and the atmospheric environment (Grannas et al., 2007;Liu et al., 2009). With respect to the climate effects, snow/ice surface has the highest albedo, which makes it the highest light reflecting surface on Earth and a key factor influencing the Earth's radiative balance. The deposition of light-absorbing particles (LAP), primarily black carbon (BC), organic carbon (OC), mineral dust (MD), and microbes, on snow reduces the snow albedo significantly and increases the absorption of solar radiation (Hadley and Kirchstetter, 2012;Skiles et al., 2018). Consequently, deposits of LAP accelerate snow melting (Hansen and Nazarenko, 2004) and affect the snow photochemistry (Zatko et al., 2013), further influencing the regional and global climate (Bond et al., 2013;Flanner et al., 2007;Jacobson, 2004). The albedo reduction and radiative forcing (RF) due to the BC and MD deposits in snow has been a subject of many field studies (Doherty et al., 2010;Huang et al., 2011;Pu et al., 2017;Shi et al., 2020;Wang et al., 2013, 2017b;Zhang et al., 2018b), remote sensing estimates (Painter et al., 2010;Pu et al., 2019), and climate models (He et al., 2014;Qian et al., 2014;Zhao et al., 2014). Darkening of snow by biological organisms, like snow algae common in high-altitude and high-latitude snowpack, has also been investigated (Cook et al., 2017a, b;Ganey et al., 2017;Lutz et al., 2014). However, yet little is known about the chemical compositions, optical

Atmospheric
Chemistry
and Physics
Discussions

Open Access

EGU

80   properties, and radiative effects of OC compounds in snow, which result from both deposition

81   of organic aerosol from natural and anthropogenic sources as well as deposits of the wind-

82   blown soil organic matter (Pu et al., 2017;Wang et al., 2013).

83   Water-soluble OC (WSOC) contributes to a large portion (10-80%) of organic aerosol

84   (Kirillova et al., 2014;Zhang et al., 2018a) and it is also widely distributed in the cryosphere.

85   The polar ice sheets and mountain glaciers store large amount of organic carbon, which provide

86   approximately 1.04 ± 0.18 TgC yr^{-1} of WSOC exported into proglacial aquatic environments

87   (Hood et al., 2015), with a substantial part of it is highly bioavailable (Singer et al., 2012;Zhou

88   et al., 2019c). WSOC components that absorb solar radiation at ultraviolet to visible (UV-Vis)

89   wavelengths are collectively termed as "brown carbon (BrC)" (Andreae and Gelencser, 2006),

90   and have become the subject of many aerosol studies (Laskin et al., 2015). The optical

91   properties of WSOC in snow started to receive attention because its important role in initiating

92   snow photochemistry (McNeill et al., 2012). Anastasio and Robles (2007) first quantified the

93   light absorption of water-soluble chromophores in Arctic and Antarctic snow samples. They

94   found that ~50% of absorption for wavelength greater than 280 nm was attributed to organic

95   chromophores. Subsequently, Beine et al. (2011) determined the light absorption of humic-like

96   substances (HULIS) in snow at Barrow, Alaska. They found that HULIS account for nearly

97   half of the total absorption by dissolved chromophores within the photochemically active

98   wavelength region (300 to 450 nm), concluding that HULIS is a major light absorber in Barrow

99   snow and that the HULIS-mediated photochemistry is probably important for the regional

100   environment. Several recent works have reported the radiative absorption of snow WSOC. Yan

101   et al. (2016) estimated amount of the solar radiation absorbed by WSOC from snow collected

Atmospheric
Chemistry
and Physics
Discussions
Open Access
EGU

102 in northern Tibetan Plateau (TP), which was 10% relative to that absorbed by BC, indicating a

103 non-negligible role of WSOC in accelerating snow and ice melting. Similar results were also

104 reported for WSOC extracted from other high-mountain areas (Niu et al., 2018;Zhang et al.,

105 2019). However, chemical characterization and optical properties of the light-absorbing

106 WSOC (aka BrC) in cryosphere is still an emerging topic. To date, no field study evaluated yet

107 the composition-specific influence of WSOC on the snow albedo reduction.

108 The fluorescence excitation-emission matrix (EEM) analysis is a sensitive, rapid, and non-

109 destructive optical spectroscopy method (Birdwell and Valsaraj, 2010) that has been used to

110 investigate the bulk composition and attribute potential sources of chromophoric WSOC in

111 aquatic ecosystems (Jaffé et al., 2014) and more recently in aerosols (Chen et al., 2016b,

112 2020;Fu et al., 2015;Mladenov et al., 2011;Wu et al., 2019b). Based on parallel factor

113 (PARAFAC) analysis, contributions from main fluorescent components such as different

114 fractions of HULIS and protein-like substances (PRLIS) can be quantitatively evaluated

115 (Stedmon and Bro, 2008), indicating plausible sources of WSOC in aquatic (Murphy et al.,

116 2008) and atmospheric samples. The chemical interpretations of PARAFAC-derived

117 components are relatively well characterized for aquatic WSOC, but it may not be simply

118 applied to WSOC in snow because their sources and geochemical processes are highly different

119 (Wu et al., 2021).

120 High resolution mass spectrometry (HRMS) interfaced with soft electrospray ionization

121 (ESI) can help to decipher complexity of WSOC, providing explicit description of its

122 individual molecular components (Qi et al., 2020). Thousands of individual organic species

123 with unambiguously identified elemental composition can be detected at once by ESI-HRMS

124 due to its high mass resolving power, mass accuracy, and dynamic range (Nizkorodov et al.,

125 2011;Noziere et al., 2015). Combined with a high-performance liquid chromatography (HPLC)

126 separation stage and photodiode array (PDA) detector, the integrated HPLC-PDA-HRMS

127 platform enables separation of WSOC components into fractions with characteristic retention

128 times, UV−vis spectra, and elemental composition. Correlative analysis of these multi-modal

129 data sets facilitates comprehensive characterization of chromophores present in complex

130 environmental mixtures (Laskin et al., 2015;Lin et al., 2016, 2018;Wang et al., 2020a).

131 Presently, HRMS studies of WSOC exist in the cryosphere are still limited to the snow/ice in

132 polar regions (Antony et al., 2014, 2017;Bhatia et al., 2010) and mountain glaciers in the Alps

133 (Singer et al., 2012) and on the TP (Feng et al., 2016;Spencer et al., 2014;Zhou et al., 2019a)

134 that with perennial snowpack. For the regions mentioned above, WSOC in snow/ice samples

135 is dominated by proteins- or lipids-like compounds from autochthonous microbial activity with

136 high bioavailability. Whereas, snow in northwestern China is seasonal, the snowpack persists

137 for 3-6 months annually, and its composition is substantially influenced by local soil dust and

138 deposited aerosols from both natural and anthropogenic sources (Pu et al., 2017). Therefore,

139 the chemical compositions and optical properties of WSOC from this area snowpack is likely

140 different from those reported for the remote regions with more persistent snow coverage.

141 In this study, seasonal snow samples were collected across the northern Xinjiang region

142 of China, in January 2018. We investigate the optical and molecular characteristics of WSOC

143 using a range of analytical techniques, including UV-Vis absorption spectrophotometry, EEM,

144 and HPLC-ESI-HRMS. Furthermore, based on the measured optical properties and

145 concentrations of snow impurities, as well as the physical properties of snow at each site, we

146   calculate for the first time extent of RF attributed to WSOC in snow.

147

2   Methods

2.1 Sample collection

150   Snow samples were collected from 28 sites in Xinjiang, northwestern China during a road

151   trip in January 2018. The area map and sampling locations are shown in Fig. 1a. The sampling

152   sites were numbered in chronological order and with numbering scheme adopted from our

153   previous campaigns (Pu et al., 2017;Wang et al., 2013, 2017b;Ye et al., 2012). The sampling

154   sites were classified into four groups based on their geographical location and proximity to

155   urban areas: urban/industrial (U) sites (no. 106-118, and 131), rural/remote (R) sites (no. 119,

156   121-125, and 127-130), soil-influenced (S) sites (no.104, 105, and 126), and site 120. The U

157   sites were located north of Tianshan Mountains, near major cities in Xinjiang area. These sites

158   were more likely influenced by local anthropogenic emissions (Pu et al., 2017). The rest of the

159   sites were assigned to R group, most of them were from desert area or barren grasslands located

160   at least ~50-100 km from major cities; hence, they were mostly influenced by natural sources.

161   The S sites are a subgroup of the R group, they correspond to specific locations where the

162   snowpack was visibly patchy and shallow, so local soil could be blown into snow by strong

163   winds. For the S samples, the coarse mineral particles of yellow/brown color were clearly seen

164   on the filters following snow water filtration (Fig. S1), consistent with the expected high

165   loadings of soils at these sites. Out of R group, a sample from site 120 was considered

166   separately because it showed composition and optical characteristics inconsistent with all other

167   samples. For instance, it had very low BC concentration but highest WSOC concentration

168   among all the samples; hence, it is discussed separately.

169
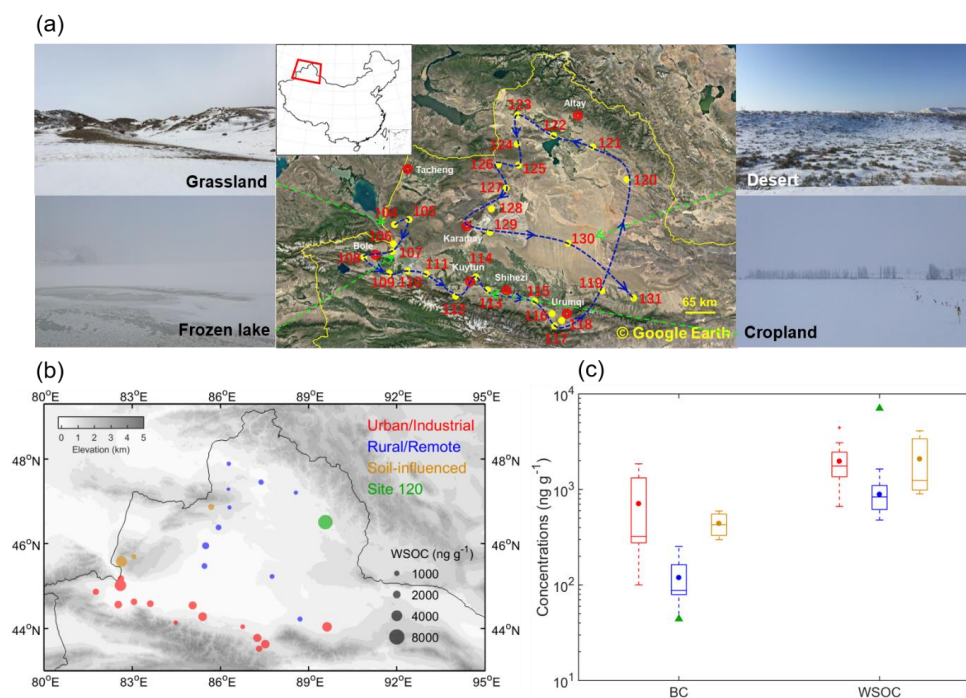
Figure 1. (a) Sampling locations and site numbers with photographs for typical land use types of sampling

sites. (b) Spatial distribution of WSOC concentrations in snow. Sampling sites are divided into four groups

indicated by different colors. The bubble sizes are proportional to the WSOC concentrations. (d) Variations

of BC and WSOC concentrations among four groups of sites. The boxes denote the 25th and 75th quantiles,

and the horizontal lines represent the medians, the averages are shown as dots; the whiskers denote the

maximum and minimum data within 1.5 times the interquartile range, and the data points out of this range

are marked with crosses (+).

178

179   Details of the sampling procedures can be found elsewhere (Wang et al., 2013) and they

180   are briefly described here. The snow sampling sites were selected at least 20 km from cities

181   and villages and at least 1 km upwind of the approach road or railway, such that the influence

182   from single-point very local sources were minimized and the samples would rather reflect

183   conditions of large regional areas. The snow samples were collected in sterile plastic bags

184   (Whirl-Pak, Nasco, WI, USA) using clean, stainless steel utensils and by scooping ~ 3 L of

185   snow every 5 cm from top to bottom at each site, resulting in ~600 mL volume of melted snow

186   water. Snow depths, snow density, and snow temperature were also measured for each snow

187   pit. All collected samples were then stored in a freezer (< -20 °C) until further processing.

188

189   **2.2 Chemical species analysis**

190   The snow samples were melted under room temperature and immediately filtered by

191   Polytetrafluoroethylene (PTFE) syringe filters with pore size of 0.22 μm (Thermo Fisher, Inc.)

192   to remove insoluble solids. Obtained filtrates were then used for the measurements of

193   concentrations of soluble inorganic ions, mass loadings of WSOC, acquisition of bulk UV-Vis

194   absorption and EEM spectra, and molecular characterization using HPLC-ESI-HRMS

195   platform.

196   The major inorganic ions (Na^+, NH_4^+, K^+, Mg^{2+}, Ca^{2+}, Cl^-, SO_4^{2-}, and NO_3^-) were

197   measured by an ion chromatography system (Dionex 600, Thermo Scientific, MA, USA) using

198   an IonPac AS22 column for anions and an IonPac CS12A column for cations. The detection

199   limits for all inorganic ions are greater than 0.05 mg L^{-1}. The concentrations of WSOC were

200   analyzed by a total organic carbon analyzer (Aurora 1030W, OI Analytical, TX, USA). Each

201   measurement was done in triplicate, the average values of each group of samples after blank

202   subtraction are presented in Table S1. The detection limit and relative standard deviation of

203 measurements were 2 ppb and 1%, respectively.

204   The BC concentrations in snow were measured by a custom-developed two-sphere

205 integration (TSI) spectrophotometer (Wang et al., 2020b), and have been reported by Shi et al.

206 (2020). The distribution of BC concentrations in snow samples is also shown in Fig. S2.

207

208 **2.3 UV-Vis absorption and fluorescence EEM spectroscopic measurements**

209   The UV-Vis absorption and fluorescence EEM spectra were recorded simultaneously by

210 an Aqualog spectrofluorometer (Horiba Scientific, NJ, USA) in a 1 cm quartz cuvette. The

211 excitation wavelengths for EEM were 240 to 600 nm in intervals of 5 nm and were the same

212 for UV-Vis spectrum acquisition. The fluorescence emission range was 250 to 825 nm in 5 nm

213 intervals with an integration time of 0.5 s. An ultrapure water (18.2 MΩ cm) was used for blank

214 measurement, subtracted from all sample spectra.

215   The absorbance at 600 nm was subtracted from the whole spectrum to correct the

216 scattering effects and baseline shifts of the instrument (Chen et al., 2019). The BrC mass

217 absorption coefficients (MAC; m^2 g^{-1}) related to WSOC contributions were calculated by:

218 $MAC_{BrC}(\lambda) = \frac{\ln(10) \cdot A(\lambda)}{c_{WSOC} \cdot L}$ (1)

219 Where λ is the wavelength, A is the base-10 absorbance measured by the spectrophotometer,

220 C_{WSOC} (mg L^{-1}) is the concentration of WSOC, L is the cuvette path length (0.01 m). To

221 characterize the wavelength dependence of MAC_{BrC}, absorption Ångström exponents (AAE)

222 were determined by a power-law regression (Kirchstetter et al., 2004):

223 $MAC(\lambda) = k \cdot \lambda^{-AAE}$,   (2)

224 where k is a constant related to WSOC concentrations. To exclude absorption due to inorganic

Atmospheric
Chemistry
and Physics
Discussions
Open Access
EGU

225 chromophores (e.g., nitrate), the *AAE* values were derived from the power law fits limited to

226 the range of 330- 400 nm ($AAE_{330-400}$) (Yan et al., 2016).

227 Processing of the EEM data followed the protocols described elsewhere (Zhou et al.,

228 2019b). Briefly, the raw EEM data sets were first background subtracted to remove the water

229 Raman scatter peaks, then the inner filter effect was corrected (Kothawala et al., 2013). The

230 fluorescence intensities were normalized to water Raman unit (RU) (Lawaetz and Stedmon,

231 2009). The processed EEM data was analyzed by the PARAFAC model in the manner similar

232 to our previous report (Zhou et al., 2019b). In this study, the PARAFAC modeling was

233 conducted using drEEM toolbox (version 0.2.0, http://models.life.ku.dk/drEEM) (Murphy et

234 al., 2013). According to the analysis of residual errors of 2- to 7- component models and split

235 half analysis, a 3-component model was selected. Only 2- and 3-component models have

236 passed the split-half analysis with the "S4C6T3" split scheme (Fig. S3) (Murphy et al., 2013).

237 Moreover, the sum of residual error decreased significantly when the number of components

238 increased from 2 to 3 (Fig. S4). The spectra of derived fluorescent components appeared

239 consistent with those commonly found in other studies (Table S2).

240

241 **2.4 HPLC-ESI-HRMS Molecular Analysis and data processing**

242 The WSOC extracts were desalted and concentrated through solid phase extraction (SPE)

243 method using DSC18 cartridges (Supelco, Millipore Sigma, PA, USA). The cartridges were

244 conditioned and equilibrated by one-column volume (~3 mL) of acetonitrile (ACN, Optima,

245 LC-MS grade, Fisher Scientific Inc.) and one-column volume of water (Optima, LC-MS grade,

246 Fisher Scientific Inc.), respectively. To increase the efficiency of SPE, the sample was acidified

247   to pH $\approx$ 2 using HCl (Lin et al., 2010), and 3 mL of acidified sample flowed through the

248   cartridge at a low flow rate of 1-2 drops per second. Salts and other unretained compounds

249   (e.g., small molecular acids and carbohydrates) were first washed out by one-column volume

250   of water, and the analyte retained on the cartridge was then eluted by two-column volumes of

251   ACN. The efficiency of SPE was evaluated by measuring the UV-Vis absorption before and

252   after elution and ensured the good recovery of analytes (Text S1). The ACN eluents were

253   concentrated to 150 μL under a gentle stream of pure N_2, and then diluted by adding 150 μL of

254   ultrapure water. Finally, the reconstituted extracts were blown down to 200 μL prior to HPLC

255   analysis.

256   The obtained extracts were analyzed using a Vanquish HPLC system coupled to a Q

257   Exactive HF-X Orbitrap HRMS with an IonMAX ESI source (all from Thermo Scientific Inc.).

258   The HPLC separation was performed on a Phenomenex Luna C18 revised-phase column (2

259   mm × 150 mm, 5 μm particles, 100 Å pores). A gradient elution was performed at a flow rate

260   of 200 μL/min by an A + B binary mobile phase system: (A) water with 0.05% v/v formic acid

261   and (B) acetonitrile with 0.05% v/v formic acid (Optima, LC-MS grade, Fisher Scientific Inc.).

262   The elution protocol was 0−3 min hold at 90% A, 3−90 min linear gradient to 0% A, 90-100

263   min hold at 0% A, and then 100−130 min hold at 90% A to recondition the column for the next

264   sample. The column temperature was maintained at 25 °C and the sample injection volume

265   was 25 μL. The UV-vis absorption of eluted chromophores was recorded by a PDA detector

266   over the wavelength range of 200 to 700 nm. Correlation analysis between PDA and MS peaks

267   and relative absorption of different chromophore fractions will be discussed in an upcoming

268   paper. For ESI-HRMS analysis, the following settings were used: 45 units of sheath gas, 10

269   units of auxiliary gas, 2 units of sweep gas, a spray voltage of 3.5 kV, a capillary temperature

270   of 250 °C, and a sweep cone was used. The mass spectra were acquired at a mass range of 80–

271   1,200 Da at mass resolving power of $\Delta m/m$ = 240,000 at m/z 200. Mass calibration was

272   performed using commercial calibration solutions (PI-88323 and PI-88324, Thermo Scientific)

273   for ESI(+/-) modes.

274   The raw experimental data files were acquired by Xcalibur software (Thermo Scientific

275   Inc.). The HPLC-ESI-HRMS data sets were preliminary processed using an open source

276   software toolbox, MZmine 2 (http://mzmine.github.io/), to perform peak deconvolution and

277   chromatogram construction (Myers et al., 2017;Pluskal et al., 2010). The background

278   subtraction and formula assignment were performed using customized Microsoft Excel macros

279   (Roach et al., 2011). The formulas were assigned based on first- and second-order Kendrick

280   mass defects and a MIDAS formula calculator (http://magnet.fsu.edu/~midas/). $[M + H]^+$, [M

281    $+ Na]^+$, and $[M − H]^-$ ions were assumed to identify products detected in ESI+ and ESI- modes,

282   respectively. Besides, adduct ions were also identified and removed using a homemade

283   MATLAB script (Text S2). The molecular formulas were assigned using the following

284   constraints: $1 \leq C \leq 50$, $1 \leq H \leq 100$, $N \leq 5$, $O \leq 50$, $S \leq 1$, and $Na \leq 1$ (ESI+ only) and mass

285   tolerance of <3.0 ppm. Furthermore, to eliminate the formulas not likely to be observed in

286   nature, the elemental ratio limits of $0.3 \leq H/C \leq 3.0$, $0.0 \leq O/C \leq 3.0$, $0.0 \leq N/C \leq 1.3$, $0.0 \leq$

287    $S/C \leq 0.8$ (Lin et al., 2012;Wang et al., 2018) were applied. The double-bond equivalent (DBE)

288   values of the neutral assigned species $C_cH_hO_oN_nS_s$ were calculated using the equation:

289    $$DBE = c - \frac{h}{2} + \frac{n}{2} + 1 \qquad\qquad (3)$$

290   The aromaticity index (AI) is a conservative criterion for the unequivocal identification of

14

291   aromatic and condensed aromatic structures in natural organic matter calculated as (Koch and

292   Dittmar, 2006, 2016):

293    $AI = \frac{1 + c - o - s - 0.5(h+n)}{c - o - n - s}$,   (4)

294    $AI > 0.5$ and $AI \geq 0.67$ are unambiguous minimum thresholds for the presence of aromatic and

295   condensed aromatic structures in a molecule, respectively. If either the numerator or

296   denominator in Eq. (4) equals to 0, then AI is assigned with 0 value.

297   The intensity (I^*) weighted molecular weight (MW_w) and other characteristic molecular

298   parameters of H/C (H/C_w), O/C (O/C_w), DBE (DBE_w), DBE/C (DBE/C_w), and AI (AI_w) were

299   calculated using Eq. (5):

300    $X_w = \frac{\sum(I_i^* \cdot X_i)}{\sum I_i^*}$,   (5)

301   where X_w represents any of the weighted parameters introduced above; I_i^*, and X_i are the

302   corresponding intensity and the molecular parameter values calculated for each assigned

303   species i, respectively.

304

305   **2.5 Snow Albedo Modeling and Radiative Forcing Calculations**

306   The spectral snow albedo was calculated by the Snow, Ice, and Aerosol Radiative

307   (SNICAR) model (Flanner et al., 2007), which accounts for the radiative transfer in the

308   snowpack based on the theory from Wiscombe and Warren (1980) and the two-stream,

309   multilayer radiative approximation (Toon et al., 1989). The input parameters required for the

310   SNICAR model are snow depth, snow density, effective snow grain size, solar zenith angle,

311   and impurity concentrations. Snow depth and density were measured in the field. The effective

312   snow grain size was retrieved from the filed-measured spectral albedo, and detailed

313   information can be found in our previous study (Shi et al., 2020). The solar zenith angle was

314   calculated using the site location and sampling date for each site. The input values of

315   parameters for the SNICAR model are summarized in Table S3.

316   To evaluate influence of BrC attributed to WSOC on the snow albedo, optical properties

317   of BrC material such as single scattering albedo (*SSA*), asymmetry factor (*g*), and mass

318   extinction coefficient (*MEC*) are needed as inputs for simulation. These parameters were

319   calculated by Mie theory, approximating WSOC as an ensemble of small BrC particles

320   distributed evenly in the snowpack. The input variables required for Mie calculation are

321   complex refractive index ($RI = n - ik$) and particle size parameter ($x = \pi d/\lambda$). The diameter of

322   individual particles (*d*), density (ρ), and the real part (*n*) of *RI* of WSOC were assumed to be

323   150 nm, 1.2 g cm^{-3}, and 1.55 (constant in the UV-Vis range), respectively (Chen and Bond,

324   2010;Lu et al., 2015b). The imaginary part (*k*) of *RI* was calculated as (Sun et al., 2007):

325     $k(\lambda) = \frac{MAC \cdot \rho \cdot \lambda}{4\pi}.$ (6)

326   Then, *SSA*, *g*, and extinction cross-section (Q_{ext}) were derived from Mie code

327   (https://omlc.org/software/mie/), and the obtained values were then used to calculate *MEC* as

328   (Seinfeld and Pandis, 2016):

329     $MEC = \frac{\pi d^2/4 \cdot Q_{ext}}{\pi d^3/6 \cdot \rho}.$ (7)

330   The spectral albedo (α_λ) was calculated for the scenarios of pure snow and BC/BrC-

331   contaminated snow. After that, the broadband albedo (α) of each scenario need to be

332   determined to calculate the broadband albedo reduction ($\Delta\alpha$) and *RF* due to different types of

333   impurities. α was derived by integration of α_λ over the wavelength range of 300 to 1500 nm

334   weighted by the incoming solar irradiance $S(\lambda)$.

335     $\alpha = \frac{\int_{300}^{1500} \alpha_\lambda S(\lambda) d\lambda}{\int_{300}^{1500} S(\lambda) d\lambda}.$ (8).

336   The incoming solar irradiance were simulated by Coupled Ocean-Atmosphere Radiative

337   Transfer (COART) model (https://cloudsgate2.larc.nasa.gov/jin/coart.html) (Jin et al., 2006)

338   for each site under clear sky assumption, therefore the calculated RF can be considered as

339   upper limits.

340   The RF resulted from either BC or BrC in snow ($RF_{BC,BrC}$) were calculated by multiplying the

341   downward shortwave solar radiation flux at surface by $\Delta\alpha_{BC,BrC}$ (Painter et al., 2013):

342     $RF_{BC,BrC} = E \cdot \Delta\alpha_{BC,BrC},$ (9)

343     $\Delta\alpha_{BC,BrC} = (\alpha_{pure\ snow} - \alpha_{BC,BrC}),$ (10)

344   where E is the average-daily downward shortwave solar radiation flux acquired from NASA's

345   Clouds and the Earth's Radiant Energy System (CERES) product "CERES SYN1deg"

346   (https://ceres.larc.nasa.gov/products.php?product=SYN1deg). $\alpha_{pure\ snow}$ and $\alpha_{BC,BrC}$ are the

347   broadband albedo of pure snow and BC or BrC contaminated snow, respectively.

348

349   **3   Results and Discussions**

350   **3.1 Characteristics of chemical species**

351   Figure 1b shows mass concentrations of WSOC measured in the snow samples, illustrating

352   their broad range from 478 to 7069 ng g^{-1} with an average of 1775±1424 ng g^{-1} (arithmetic

353   mean ± 1 standard deviation, and same below). The U and the S sites showed higher

354   concentrations with averages of 1968±953 ng g^{-1} and 2082±1438 ng g^{-1}, respectively, while

355   the value of R sites (885±328 ng g^{-1}) was approximately a factor of two lower (Table S1). Of

356   note, the WSOC concentrations in U and S samples   reported here are significantly higher

357   than those found in the snow and ice from polar regions (~40 – 500 ng g^{-1}) (Fellman et al.,

358   2015;Hagler et al., 2007a,b;Hood et al., 2015), glaciers on the European Alps (~100 – 300 ng

359   g^{-1}) (Legrand et al., 2013;Singer et al., 2012), and the remote TP region (~150 – 700 ng g^{-1})

360   (Yan et al., 2016). However, our reported WSOC mass concentrations are in the same range as

361   those in the fresh snow samples collected from Laohugou (LHG) glacier, northern TP (2000 –

362   2610 ng g^{-1}) (Feng et al., 2018). It follows that in addition to the snow and glaciers from polar

363   or alpine regions, the seasonal snow in Northern Xinjiang is also an important organic carbon

364   source for the covered ecosystems.

365   As shown in Fig. 1c, the U sites were also associated with the highest BC concentrations

366   among all four groups (mean: 707±651 ng g^{-1}). Furthermore, the mass contributions of sulfate

367   ions at U sites (Table S1, mean: 33%±7%), which is a commonly-used marker for fossil fuel

368   burning (Pu et al., 2017), were approximately twice as high as those from the other sites. All

369   these results indicate strong influence from anthropogenic pollution sources, explaining high

370   WSOC loadings at U sites. For the S sites, HULIS from local soil may dominate the WSOC

371   composition. For example, snow at site 104 was patchy and thin (Fig. 1a, grassland), the local

372   black soil can be lifted by winds and then redeposited and mixed with snow. The assumption

373   of soil contributions agrees with observed high mass contribution of calcium ions in S samples

374   (mean: 50%±4%, see Table S1). Although WSOC concentrations in R samples were relatively

375   low, they were still higher than most of the values from high-altitude or high-latitude regions

376   of previous studies. It might be explained by two reasons: (1) more intensive anthropogenic

377   emissions in the northern Xinjiang region; (2) there was little snowfall during 2018 campaign;

378   therefore, pollutants had been potentially accumulated on the snow surface by sublimation and

Atmospheric
Chemistry
and Physics
Discussions

379   dry deposition (Doherty et al., 2010). The sample from site 120 is discussed separately as it

380   exhibited the highest WSOC concentration (7069 ng g^{-1}) and almost the lowest BC

381   concentration (44 ng g^{-1}) out of all samples analyzed in this work. The potential sources of

382   WSOC from site 120 sample will be discussed in section 3.3.

383

384   **3.2 Bulk light-absorbing and fluorescence properties**

385   The average MAC_{BrC} spectra of WSOC from different groups of samples are shown in Fig.

386   2a. The average MAC_{BrC} at 365 nm (MAC_{365}) of S samples (0.94±0.31 m^2 g^{-1}) was significantly

387   higher than those of U (0.39±0.11 m^2 g^{-1}) and R (0.38±0.12 m^2 g^{-1}) samples, respectively (Table

388   S1). The information on MAC_{BrC} related to WSOC in snow and ice is yet very scarce in

389   literature. The MAC_{365} values of U and R samples are comparable with the results reported for

390   snow collected from Barrow, Alaska (0.32±0.24 m^2 g^{-1}) (Zhang et al., 2020), but slightly lower

391   than those of snow WSOC from Chinese Altai Mountains (0.45±0.35 m^2 g^{-1}) (Zhang et al.,

392   2019) and HULIS extracted from Arctic snow (~0.5 m^2 g^{-1}) (Voisin et al., 2012). The snow/ice

393   samples from LHG glacier on the TP (Yan et al., 2016) presented a higher average MAC_{365} (1.3

394   – 1.4 m^2 g^{-1}) than the S samples; they also indicated large contribution of dust-derived organics.

395   The relative lower values of MAC_{365} measured for U samples might be explained by

396   photobleaching of WSOC during aging on the snow surface (Yan et al., 2016;Zhang et al.,

397   2019). Due to the stronger wavelength dependence of WSOC from U samples ($AAE_{330-400}$:

398   6.0±0.8 vs. 5.4±0.7 for U and R sites, respectively), their MAC values at shorter wavelength

399   of 300 nm were higher compared to those of R samples. For example, the averages of MAC_{300}

400   were 1.32±0.24 m^2 g^{-1} and 1.02±0.21 m^2 g^{-1} for U and R samples, respectively (Table S1). The

401    $AAE_{330\text{-}400}$ of our samples were in the range of 4.3 to 12.3 (mean: 6.0±1.5), and S sites had a

402   higher average of 6.4±0.3 than those corresponding to U and R samples. The highest $AAE_{330\text{-}400}$

403    $_{400}$ = 12. 3 was found for WSOC from site 120 sample, and its UV-Vis spectrum also exhibited

404   an unusual spectral shape with a well-defined spectral feature observed between 300 and 350

405   nm. Similar feature was reported in: (1) cryoconite samples collected from TP glaciers (Feng

406   et al., 2016), which may be attributed to mycosporine-like amino acids (MAAs) produced by

407   microorganisms (e.g. fungi, bacteria, and algae) (Elliott et al., 2015;Shick and Dunlap, 2002);

408   (2) Plant-derived (e.g., corn, hairy vetch, or alfalfa) water extractable organic matter containing

409   phenolic carboxylic compounds (He et al., 2009).
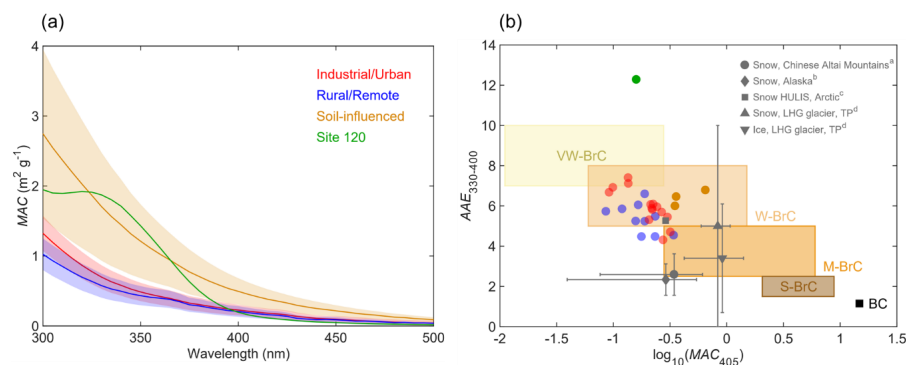
411   **Figure 2.** (a) The average MAC spectrum of BrC attributed to WSOC in each group (solid lines, denoted by

412   different colors), the shaded areas represent one-time standard deviations. (b) Plot of the optical-based BrC

413   classification scheme (Saleh, 2020) in the $\log_{10}(MAC_{405}) - AAE_{330\text{-}400}$ space. The shaded areas represent very

414   weakly absorbing BrC (VW-BrC), weakly absorbing BrC (W-BrC), moderately absorbing BrC (M-BrC),

415   and strongly absorbing BrC (S-BrC). BC is also shown for reference (Bond and Bergstrom, 2006). Grey

416   marks indicate the data from literatures for snow/ice samples from Chinese Altai Mountains ([a] Zhang et al.,

417   2019), Alaska ([b] Zhang et al., 2020), Arctic ([c] Voisin et al., 2012, AAE is calculated for 300-400 nm), LHG

418   glacier on the TP ([d] Yan et al., 2016). Error bars denote the standard deviations of AAE and MAC values.

419   Figure 2b shows MAC and $AAE_{330-400}$ values measured for BrC attributed to WSOC from

420   our samples in the context of an optical-based classification of BrC presented recently by Saleh

421   (2020). The optical properties characterizing the BrC classes are expected to be associated with

422   their corresponding physicochemical properties (i.e. molecular sizes, volatility, and solubility).

423   Most of our samples and HULIS in Arctic snow (Voisin et al., 2012) fall into the region of

424   weakly absorbing BrC (W-BrC). The WSOC in snow/ice from Alaska, Chinese Altai

425   Mountains, and LHG glaciers were assigned to moderately absorbing BrC (M-BrC) but with

426   broader ranges, likely indicating higher molecular variability. These results provide a useful

427   framework for representing snow BrC optical properties in climate models.

428   Three fluorescent components (i.e., C1, C2, and C3) were identified by PARAFAC

429   analysis (Fig. 3a). The peak positions of each component are summarized in Table S2. C1

430   (HULIS-1) is a type of terrestrial-derived humic fluorophore with long emission wavelengths,

431   commonly reported for samples of terrestrial aquatic systems and highly-oxygenated organic

432   aerosols (Chen et al., 2016a;Stedmon et al., 2003). C2 (HULIS-2) is usually recognized as

433   HULIS from marine sources (Coble, 1996) or phytoplankton degradation in fresh water (Zhang

434   et al., 2010), and it was also detected in anthropogenic wastewater (Stedmon and Markager,

435   2005) or industrial-sourced aerosol (Chen et al., 2020). C3 is a class of PRLIS (tyrosine-like)

436   widely found in terrestrial organics (Wu et al., 2020;Zhang et al., 2010;Zhao et al., 2016)

437   related to labile organic matter produced from microbial processes (Coble et al., 1998).

438
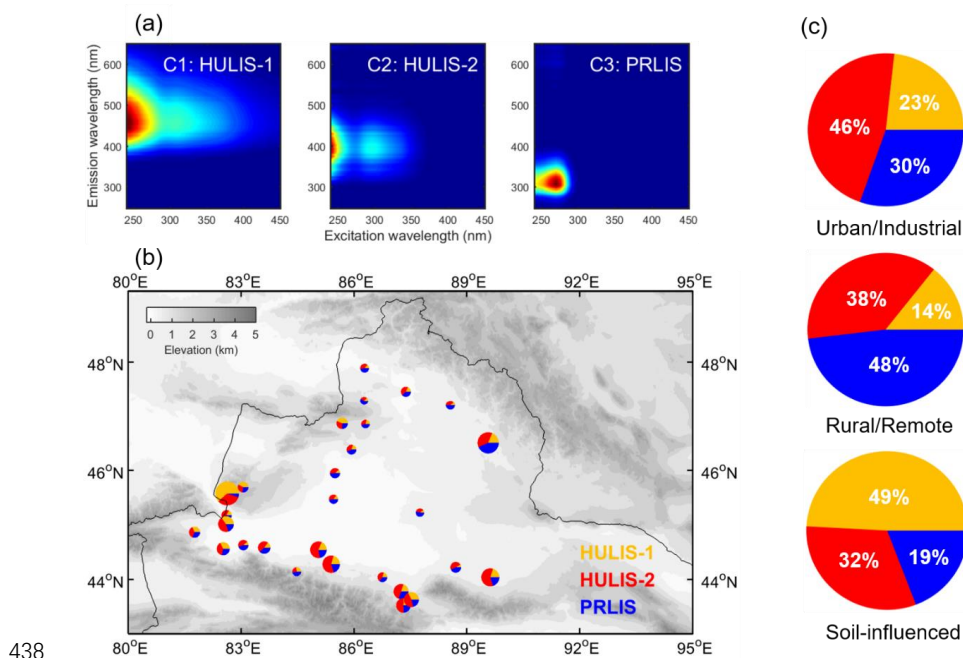
Figure 3. (a) The fingerprints of three fluorescent components identified by PARAFAC analysis. (b)

Relative contributions of three components to total fluorescence at each site. HULIS-1, HULIS-2, and

PRLIS are represented in yellow, red, and blue, respectively. The size of each pie is proportional to the total

fluorescence intensity at each site. (c) The average contributions of three components in different groups of

samples.

As shown in Figs. 3b and 3c, the relative intensities of three fluorescent components were

highly variable among different groups of samples, suggesting systematic substantial

differences in their chemical compositions. HULIS-1 dominates in the S samples, where it

accounts for ~49% of the total fluorescence (Table S1). In addition, the relative intensities of

HULIS-1 are positively correlated with the mass fractions of calcium ion (r=0.73, p<0.01,

Table S4). These results suggest terrestrial origin (soil dust) of HULIS-1, which is consistent

451   with previous studies of water systems and aerosols (Chen et al., 2016a,2020;Stedmon et al.,

452   2003). A strongly negative correlation between the contributions of HULIS-1 and nitrate mass

453   fractions is found as well (r=-0.68, p<0.01), reflecting the potential important role of HULIS

454   in snow nitrate photochemistry (Bartels-Rausch et al., 2010;Grannas et al., 2007). HULIS-2

455   dominates U samples with an average contribution of ~46%. Given the significantly positive

456   correlation between the contributions of HULIS-2 and mass fractions of sulfate ion (r=0.51,

457   p<0.01), the primary relevance of anthropogenic emissions for HULIS-2 is confirmed. The R

458   samples show significant contribution of PRLIS fluorophore (mean: 48%±6%), indicating an

459   important role of microbial processes in the composition of WSOC in these samples. This

460   observation is in line with previous studies showing that snow is not only an active

461   photochemical site, but also a biogeochemical reactor in the nitrogen cycling (Amoroso et al.,

462   2010). Amoroso et al. (2010) found that nitrate and nitrite ions in snow collected from Ny-

463   Ålesund, Norway, were most likely from microbial oxidation of ammonium ions. Therefore,

464   the significant correlation (r=0.78, p<0.01) between relative intensities of PRILS and nitrate

465   mass fractions might be interpreted by: (1) low anthropogenic emissions and local soil dust

466   import (Less contributions of sulfate and calcium ions) and (2) potential metabolic production

467   of nitrate/nitrite in snow at R sites. Further research is needed to investigate this hypothesis in

468   more detail. Of interest, EEM from site 120 sample cannot be modeled well by PARAFAC

469   (Fig. S5) because of the uncommon spectroscopic feature with emission and excitation

470   wavelengths of 315 nm and 452 nm, respectively. This feature is possibly attributed to: (1)

471   NADH (Nicotinamide adenine dinucleotide) -like compounds, which is an indicator for the

472   metabolism of organisms (Pöhlker et al., 2012) or (2) plant-derived water extractable organic

473 matter (Hunt and Ohno, 2007), e.g., corn. This result suggests strong influence from either

474 microbial activity or plant-sourced organics in snow at site 120, which is also consistent with

475 the UV-Vis spectrum shape.

476

477 **3.3 Molecular-level insights into composition of WSOC from snow samples**

478 **3.3.1 General HRMS characteristics**

479 Numbers of assigned species ranged from 561 to 1487 and from 339 to 1568 for ESI+ and

480 ESI- modes, respectively, suggesting high variations of molecular components of WSOC in

481 the snow samples from northern Xinjiang. The assigned peaks accounted for majority (49% -

482 68%) of all detected MS peaks. Due to the different ionization mechanisms between positive

483 and negative ESI (Lin et al., 2012), only small amounts of compounds were detected in both

484 modes, accounting for approximately 15% of total assignments at each representative site (Fig.

485 S6). The assigned formulas were classified into eight categories, i.e., CHO, CHON, CHOS,

486 CHONS, CH, CHS, CHN, CHS. CHONS referred to formulas containing carbon, hydrogen,

487 oxygen, nitrogen and sulfur elements, and other categories were defined analogously. The U

488 samples had the highest number of assigned compounds among four groups of sites in both

489 ESI+ and ESI- with averages of 1113 ± 203 and 871 ± 287, respectively (Tables 1 and 2), whereas

490 the number of assigned species from S samples were lowest (mean: 727 ± 146 and 438 ± 84 for

491 ESI+ and ESI- modes, respectively), reflecting high molecular complexity of U samples. The

492 numbers of assigned formulas in this study are comparable with the assignments reported for

493 urban aerosol samples (~800-1800) (Lin et al., 2012;Wang et al., 2017a) and WSOC of LHG

494 glacier from the TP region (~700-1900) (Feng et al., 2016;Feng et al., 2018), but they are lower

495   than those of WSOC from Antarctica (~1400-2600) and Greenland ice sheets (~1200-4400)

496   (Antony et al., 2014;Bhatia et al., 2010).

497

Atmospheric
Chemistry
and Physics
Discussions

498 **Table 1.** Averages (Arithmetic Mean ± Standard Deviation) of molecular characteristics in major formula categories detected in ESI+ mode for each group of sites.

499 Numbers and percentages of formulas, intensity weighted MW_w, H/C_w, O/C_w, DBE_w, DBE/C_w, AI_w are given.

		All+	CH+	CHO+	CHON+	CHOS+	CHONS+	CHS+
U Urban/Industrial (n = 14)	Number of formulas	1113±203	48±6	460±68	249±61	121±33	135±45	43±15
	Percent of formulas (%)		4.4±0.5	41.9±5.4	22.1±1.4	10.8±1.8	11.9±2.3	3.8±1.2
	Molecular weight (Da)	231±9	146±5	207±21	211±15	329±18	294±18	257±13
	H/C_w	1.51±0.05	1.31±0.04	1.72±0.10	1.73±0.14	1.12±0.09	1.70±0.08	1.11±0.02
	O/C_w	0.19±0.04	0	0.28±0.05	0.23±0.02	0.07±0.02	0.29±0.04	0
	DBE_w	5.08±0.60	4.6±0.47	3.03±0.66	3.68±0.68	10.13±0.70	4.10±0.44	8.67±0.63
	DBE/C_w	0.34±0.03	0.44±0.02	0.24±0.04	0.34±0.07	0.49±0.05	0.35±0.04	0.51±0.01
	AI_w	0.25±0.04	0.44±0.02	0.13±0.03	0.17±0.09	0.42±0.07	0.15±0.04	0.48±0.01
R Remote/Rural (n = 10)	Number of formulas	942±166	45±11	533±81	245±51	25±15	53±13	7±3
	Percent of formulas (%)		4.7±0.8	56.8±1.9	25.9±1.5	2.6±1.5	5.6±1.1	0.7±0.2
	Molecular weight (Da)	229±10	134±11	239±12	214±17	351±21	260±20	237±30
	H/C_w	1.69±0.04	1.26±0.08	1.75±0.04	1.69±0.10	1.51±0.04	1.74±0.08	1.17±0.12
	O/C_w	0.34±0.01	0	0.39±0.01	0.27±0.02	0.10±0.05	0.26±0.02	0
	DBE_w	3.16±0.21	4.53±0.31	2.80±0.16	4.11±0.48	6.25±0.51	3.92±0.62	7.49±1.64
	DBE/C_w	0.26±0.02	0.47±0.04	0.22±0.02	0.35±0.05	0.30±0.02	0.39±0.03	0.49±0.06
	AI_w	0.12±0.03	0.47±0.04	0.07±0.03	0.18±0.06	0.19±0.03	0.15±0.04	0.45±0.07
S Soil-influenced (n = 3)	Number of formulas	727±146	27±11	407±106	186±39	34±21	33±4	7±6
	Percent of formulas (%)		3.7±0.9	55.5±4.0	25.6±0.3	5.0±3.0	4.8±1.2	1.0±0.9
	Molecular weight (Da)	218±15	138±3	215±30	188±14	330±11	290±20	220±32
	H/C_w	1.73±0.05	1.33±0.02	1.84±0.08	1.75±0.06	1.35±0.17	1.73±0.06	0.92±0.13
	O/C_w	0.33±0.04	0	0.40±0.01	0.23±0.01	0.07±0.01	0.29±0.05	0
	DBE_w	3.11±0.45	4.29±0.13	2.21±0.53	3.31±0.06	7.60±1.56	4.23±0.18	8.63±0.34
	DBE/C_w	0.25±0.03	0.44±0.01	0.18±0.03	0.32±0.03	0.38±0.09	0.36±0.02	0.61±0.07
	AI_w	0.14±0.05	0.44±0.01	0.07±0.02	0.15±0.03	0.29±0.09	0.13±0.03	0.58±0.07
Site **120**	Number of formulas	987	51	578	238	10	65	4

Table 2. Averages (Arithmetic Mean ± Standard Deviation) of molecular characteristics in major formula categories detected in ESI- mode for each group of sites. Numbers and percentages of formulas, intensity weighted MW_w, H/C_w, O/C_w, DBE_w, DBE/C_w, AI_w are given.

Group (n = 1):

Metric	All-	CHO-	CHON-	CHOS-	CHONS-	(col 6)	(col 7)
Percent of formulas (%)		5.2	58.6	24.1	1.0	6.6	0.4
Molecular weight (Da)	234	145	245	212	338	246	250
H/C_w	1.69	1.29	1.72	1.80	1.54	1.95	1.14
O/C_w	0.32	0	0.37	0.26	0.06	0.29	0
DBE_w	3.36	4.67	3.14	3.54	5.87	2.99	8.05
DBE/C_w	0.26	0.45	0.23	0.30	0.28	0.32	0.50
AI_w	0.11	0.45	0.07	0.12	0.20	0.07	0.46

Group	Metric	All-	CHO-	CHON-	CHOS-	CHONS-
U Urban/Industrial (n = 14)	Number of formulas	871±287	404±112	194±79	156±48	82±49
	Percent of formulas (%)		47.2±3.6	21.9±2.2	18.2±1.9	8.7±3.2
	Molecular weight (Da)	223±17	229±19	183±18	238±17	252±24
	H/C_w	1.48±0.09	1.57±0.06	1.00±0.14	1.68±0.08	1.55±0.15
	O/C_w	0.35±0.04	0.30±0.05	0.45±0.04	0.56±0.05	0.60±0.06
	DBE_w	4.14±0.26	3.87±0.31	5.59±0.51	3.13±0.42	4.55±0.55
	DBE/C_w	0.38±0.06	0.30±0.04	0.72±0.08	0.29±0.04	0.46±0.08
	AI_w	0.19±0.07	0.12±0.04	0.54±0.09	0.05±0.02	0.14±0.06
R Rural/Remote (n = 10)	Number of formulas	537±92	266±35	107±21	100±29	34±16
	Percent of formulas (%)		50.0±4.0	19.9±1.9	18.3±2.3	6.0±2.2
	Molecular weight (Da)	215±21	216±28	180±12	241±22	241±27
	H/C_w	1.44±0.07	1.54±0.10	1.03±0.16	1.76±0.10	1.52±0.13
	O/C_w	0.39±0.06	0.37±0.07	0.42±0.04	0.58±0.08	0.65±0.07
	DBE_w	4.09±0.31	3.70±0.65	5.43±0.69	2.68±0.86	4.30±0.79
	DBE/C_w	0.42±0.05	0.33±0.05	0.72±0.10	0.25±0.06	0.49±0.07
	AI_w	0.26±0.05	0.13±0.05	0.60±0.14	0.04±0.04	0.16±0.06

S Soil-influenced (n = 3)	Number of formulas	438±84	245±53	85±18	69±9	22±6
	Percent of formulas (%)		55.6±2.0	19.3±0.8	16.1±2.2	5.0±0.7
	Molecular weight (Da)	206±3	195±11	212±27	249±15	228±11
	H/C_w	1.53±0.01	1.53±0.01	1.48±0.23	1.47±0.22	1.76±0.2
	O/C_w	0.41±0.02	0.42±0.03	0.36±0.02	0.42±0.04	0.67±0.03
	DBE_w	3.65±0.07	3.40±0.31	4.43±1.51	4.51±1.29	3.51±0.32
	DBE/C_w	0.36±0.01	0.35±0.00	0.43±0.11	0.37±0.12	0.38±0.09
	AI_w	0.13±0.01	0.12±0.00	0.22±0.10	0.09±0.05	0.13±0.05
Site **120** (n = 1)	Number of formulas	645	391	115	88	36
	Percent of formulas (%)		60.6	17.8	13.6	5.6
	Molecular weight (Da)	280	273	316	271	396
	H/C_w	1.41	1.47	0.96	1.51	1.15
	O/C_w	0.34	0.31	0.45	0.50	0.44
	DBE_w	5.82	5.10	9.81	5.19	11.97
	DBE/C_w	0.39	0.34	0.69	0.35	0.59
	AI_w	0.15	0.10	0.51	0.13	0.26

28

Atmospheric
Chemistry
and Physics
Discussions

Open Access

EGU

506   The mass spectra plots constructed from individual samples showing integrated

507   composition of U, R, S, and site 120 samples along with the corresponding number

508   contributions from different formula categories are shown in Fig. 4. Overall, the

509   assigned formulas were mainly in the mass range of 100 to 450 Da for both ESI+ and

510   ESI-, while there were more compounds with masses lower than 100 in the ESI+ mode.

511   The relative intensities of MS features contributed by compounds in different mass

512   ranges extract more information from the mass spectra, as shown in Fig. 5. In ESI-

513   mode, the ion intensity was most abundant in the mass range of 200 to 250 Da for U

514   samples, 250 to 300 Da for R and site 120 samples, and 150 to 200 Da for S samples,

515   indicating different chemical constituents for samples from different groups. The

516   variations in terms of relative intensities for CHO- compounds were like those of all

517   species detected in ESI-. For CHON-, formulas with mass of 150 to 200 Da were

518   abundant in S samples, while other groups were dominant by formulas in the range of

519   100 to 150 Da. Sample from site 120 showed higher fractions of formulas with masses

520   larger than 300 Da, especially for CHONS- compounds. The distributions of all

521   detected compounds showed higher contributions from mass range of 300 to 350 Da in

522   ESI+ compared to ESI-. Although detection of CH compounds in ESI is uncommon,

523   some of them appear detectable in the ESI+ mode, most were associated with aromatic

524   species smaller than 150 Da (DBE≥4). Furthermore, the CHONS+ species showed

525   higher masses than CHONS-, except for the sample from site 120.
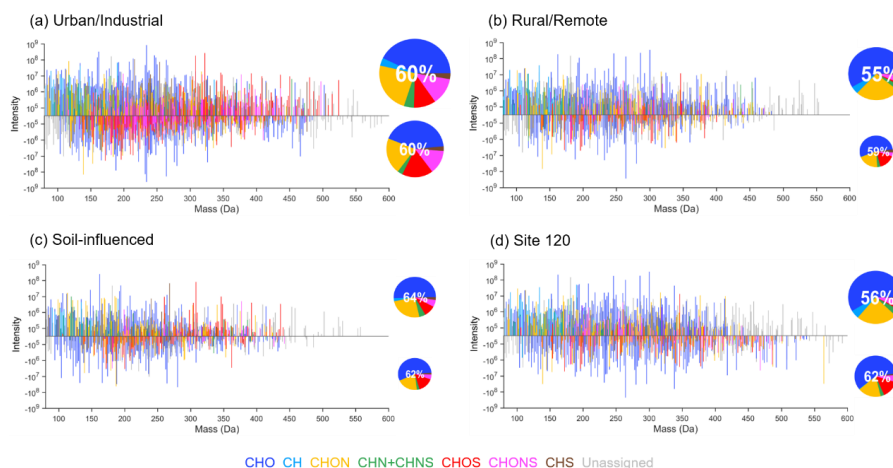
Figure 4. The reconstructed mass spectra of representative samples for four groups of sites: (a) site 114, (b) site 123, (c) site 104, (d) site 120. The data measured by ESI+/- are plotted as positive/negative intensities, respectively. The pie charts show the number contributions from different formula categories indicated by different colors, and the sizes of pie charts are proportional to the total numbers of assigned formulas detected in each sample by ESI+/-. The percentages present the ratios of assigned formula to total MS peaks. Unassigned peaks were converted into neutral mass by assuming that they were protonated in ESI+ and deprotonated in ESI-.
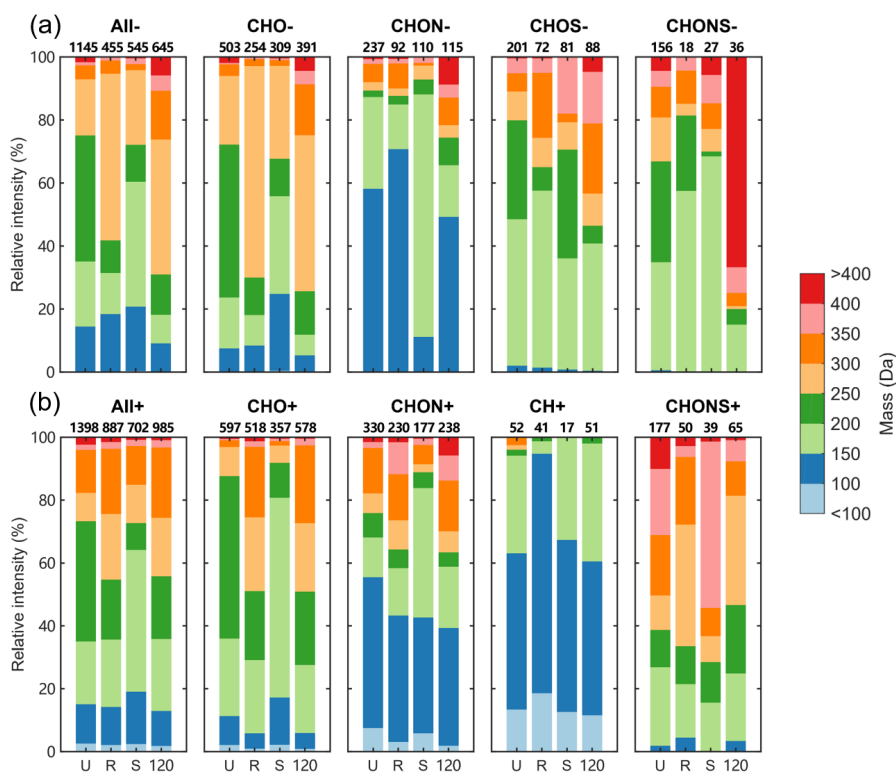
Figure 5. The distributions for relative intensities of compounds in different mass ranges in (a) ESI-
and (b) ESI+. The numbers on the top of bars indicate the number of assigned peaks in different
formula categories of each sample.

In ESI+ mode, CHO+ and CHON+ were the main components in all samples,
accounting for 35% to 61% and 20% to 28% of total formulas, respectively (Table 1).
The U samples showed the lowest CHO+ abundance (mean: 42%±5%) while the
sample from site 120 had the highest value (59%). The fractions of CHON+ species in
our samples were significantly lower than those of the aged firn/ice samples from the
TP (Feng et al., 2016,2018,2020;Spencer et al., 2014) in which WSOC showed high
bioavailability; but were comparable with the WSOC samples from fresh snow (Feng
et al., 2018,2020). These results indicate that WSOC from the snowpack in northern

Atmospheric
Chemistry
and Physics
Discussions

547   Xinjiang was more likely from atmospheric aerosol depositions rather than from

548   autochthonous sources. There were much higher contributions of S-containing

549   compounds in the U samples, e.g., CHOS+ (11%), CHONS+ (12%), and CHS+ (4%),

550   which were less abundant in other samples. These species showed low oxidation level

551   (mean O/C_w: 0.07 for CHOS+), high unsaturation degree and aromaticity (mean DBE_w:

552   10.1 and 8.7; mean AI_w: 0.42 and 0.48 for CHOS+ and CHS+, respectively), suggesting

553   that they might be reduced S-containing species with aromatic structures from

554   incomplete fossil fuel combustion (Mead et al., 2015;Wang et al., 2017a).

555   The abundance of CHO- was highest in ESI- with a range of 41% to 61%. The U

556   samples and the site 120 sample showed the lowest (mean: 47%±4%) and highest (61%)

557   fractions of CHO-, respectively. The CHON- and CHOS- compounds account for

558   roughly equal contributions with ranges of 16% to 27% and 14% to 22%, respectively.

559   The detected CHOS compounds were more abundant in ESI- than those in ESI+.

560   Furthermore, CHOS- compounds shows much higher oxidation level and lower

561   unsaturation degrees than CHOS+ (mean O/C_w: 0.55 and 0.08; mean DBE: 8.3 and 3.2

562   for CHOS- and CHOS+, respectively). These results are consistent with previous

563   ambient aerosol characterization studies (Lin et al., 2012;Wang et al., 2017a,2018), but

564   the S-containing species were not abundantly detected in the glacier samples (Feng et

565   al., 2016;Spencer et al., 2014), indicating stronger influence from anthropogenic

566   aerosols to WSOC in Xinjiang seasonal snow than those from remote areas.

567   The bulk molecular characteristics of compounds detected in ESI+ and ESI- are

568   summarized in Tables 1 and 2, respectively. The MW_w of all compounds detected in

569   ESI+ mode was 231±9 Da, 229±10 Da, 218±15 Da, and 234 Da for U, R, S, and site

570   120 samples, respectively. These values are comparable with the MW_w of urban aerosols

571   (~225 to 265 Da) (Lin et al., 2012;Wang et al., 2018), but significantly lower than those

572   of glacier samples (~360 Da to 420 Da), suggesting different compositions between

573   WSOC in seasonal snow of our study and from the literature reported glacier samples.

574   *DBE* is used to infer the unsaturation degree of individual species (McLafferty et al.,

575   1993) and *AI* is a more direct metric of their aromaticity (Koch and Dittmar, 2006,

576   2016). The U samples showed higher DBE_w and AI_w values than the other groups of

577   samples mainly due to high fractions of S-containing compounds (Table 1). In ESI-

578   mode, the MW_w of the site 120 sample was higher than the other samples (280 Da vs.

579   ~200 – 220 Da). Of note, the average MW_w of CHON- and CHONS- compounds in the

580   site 120 sample were 316 Da and 396 Da, respectively, which were approximately 100

581   Da and 150 Da higher than those from the other groups of samples. Accordingly, the

582   DBE_w of all formulas detected in the site 120 sample was the highest (5.8), the values

583   for CHON- and CHONS- were 9.8 and 12.0, respectively, which were approximately 2

584   and 3 times higher than in the other samples. These results indicate very unusual sources

585   of WSOC in the site 120 sample.

586

587   **3.3.2 Chemical species in snow WSOC**

588   The Van Krevelen (VK) diagram is a frequently used graphical method, which plots

589   the *H/C* ratios against the *O/C* ratios in molecular formulas, to qualitatively determine

590   the major chemical species in complex organic mixtures and to explore their potential

591   reaction pathways (Kim et al., 2003). The VK diagrams of four representative samples

592   detected in ESI+ and ESI- modes are shown in Fig. 6. The VK space in this study was

593   separated into seven regions according to previous studies (Feng et al., 2016;Ohno et

594   al., 2010): (1) lipids-like (*O/C* = 0−0.3, *H/C* = 1.5−2.0), (2) aliphatic/proteins-like (*O/C*

595   = 0.3−0.67, *H/C* = 1.5−2.2), (3) carbohydrates-like (*O/C*=0.67−1.2; *H/C*=1.5−2.4), (4)

596   unsaturated hydrocarbons (*O/C* = 0−0.1, *H/C* =0.7−1.5), (5) lignins/carboxylic-rich

597   alicyclic molecules (CRAMs)-like (O/C = 0.1−0.67, H/C = 0.7−1.5), (6) tannins-like

598   (O/C = 0.67−1.2, H/C = 0.5−1.5), and (7) condensed aromatics (O/C = 0−0.67, H/C =

599   0.2−0.7). In ESI+, the U samples showed the lowest O/C ratios (mean: 0.19±0.04) and

600   H/C ratios (mean: 1.51±0.05) among four groups (Table 1), which indicate low

601   oxygenation and high unsaturation degree of WSOC from U samples, likely indicating

602   their primary emission sources. Consequently, the unsaturated hydrocarbons were most

603   abundant among seven classes of species (mean: 39±15%, Table 3), most of which were

604   CHOS+ compounds (Fig. S7), then followed by lignins/CRAMs-like species (mean:

605   25±11%). These results, again, supports our assumption that anthropogenic pollution is

606   a major source of snow organics in the U region. The R samples exhibited the highest

607   fraction of aliphatic/proteins-like species among four groups (mean: 57%±4%,). This

608   type of species is widely distributed in natural dissolved organic matter detected in

609   terrestrial water systems (Lu et al., 2015a), glaciers and polar ice sheets (Antony et al.,

610   2014;Feng et al., 2016), aerosols (Ning et al., 2019;Wu et al., 2019a;Xie et al., 2020),

611   and cloud water (Bianco et al., 2018). The aliphatic/proteins-like species are commonly

612   regarded as a marker of biological-related sources, such as in-situ microbial activities

613   (Antony et al., 2017) and primary bioaerosols (e.g., plant debris, fungal spores, and

614   pollen) (Xie et al., 2020). The high contribution of aliphatic/proteins-like species in R

615   samples is consistent with the results of our EEM-PARAFAC analysis, which showed

616   that PRLIS fluorophore is the most abundant. The U samples and the site 120 sample

617   showed high contributions of lignins/CRAMs-like species, but their sources might be

618   different. The lignins/CRAMs-like species are commonly attributed to terrestrial-

619   sourced, vascular plant-derived material (Antony et al., 2014), biomolecules with

620   similar structures to sterols and hopanoids (Hertkorn et al., 2006), or secondary organic

621   aerosols from biomass burning (Xie et al., 2020). These compounds in U samples were

Atmospheric
Chemistry
and Physics
Discussions

Open Access

EGU

622 more likely from combustion of biomass materials, but those in the site 120 sample

623 might be from biogenetic sources. The S samples showed higher contributions of

624 unsaturated hydrocarbons (mean: 19%±14%,) than the R samples and the site 120

625 sample (mean: 11%±2% and 10%, respectively), which were mainly due to the CHOS+

626 compounds detected in the site 104 sample, which showed some influence by

627 anthropogenic pollution.
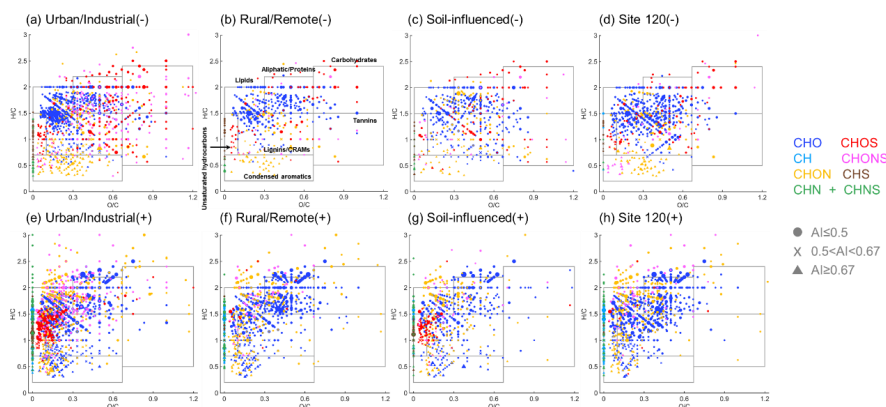
628

629 **Figure 6.** Van Krevelen diagrams of representative sample for each subgroup in (a-d) ESI- and (e-

630 h) ESI+. The boxes indicate the different classes of chemical species. Different formula categories

631 are color coded. Dots, crosses, and triangles represent non-aromatic (AI≤0.5), aromatic

632 (0.5<AI<0.67), and condensed aromatic compounds (AI≥0.67) (Koch and Dittmar, 2006),

633 respectively. The sizes of the symbols are proportional to the intensities.

634

Atmospheric Chemistry and Physics Discussions — Open Access

635

Table 3. The relative abundance of different classes of molecular species in each group of sites.

		%Lipids-like	%Aliphatic/protein-like	%Carbohydrates-like	%Unsaturated hydrocarbons	%Lignins/CRAMs-like	%Tannins-like	%Condensed aromatics
U Urban/Industrial (n = 14)	ESI+	18.2±9.1	14.6±11.7	0.2±0.1	38.8±15.3	25.3±10.9	0	2.9±2.5
	ESI-	10.8±12.6	24.3±6.7	3.6±1.0	1.1±0.4	56.3±11.6	2.5±1.2	1.4±0.4
R Rural/Remote (n = 10)	ESI+	12.2±4.0	57.1±3.7	0.7±0.2	11.3±2.2	13.5±2.8	0.1	5.1±5.4
	ESI-	9.9±6.9	27.0±8.0	4.6±0.8	2.4±1.5	50.1±16.2	2.6±1.1	3.4±3.1
S Soil-influenced (n = 3)	ESI+	14.7±2.4	46.6±21.9	0.5±0.1	18.7±14.3	13.8±4.6	0.1	5.7±1.3
	ESI-	8.8±4.9	41.1±0.7	5.2±0.8	1.4±0.1	39.0±5.4	2.8±1.7	1.7±0.1
Site 120 (n = 1)	ESI+	14.2	52.2	0.4	10.1	21.8	0.1	1.3
	ESI-	5.8	13.0	2.1	2.0	74.5	0.8	1.7

636

637

Atmospheric
Chemistry
and Physics
Discussions
Open Access
EGU

638   The relative abundances of seven chemical species to four major formula categories

639   are shown in Fig. S7. Aliphatic/proteins-like species dominated the CHO+ compounds

640   in the R and the site 120 samples, while lignins/CRAMs-like species were most

641   abundant in the U sample. The contribution of condensed aromatics to CHO+ in the S

642   sample was high, which might be from soil-derived humic acids (DiDonato et al.,

643   2016;Ikeya et al., 2015). Lipids-like species were highly enriched in CHON+, except

644   for the U samples, in which significantly higher contributions from condensed

645   aromatics were observed. The condensed aromatics have typical AI values > 0.67 and

646   low O/C ratios which might be indicative of nitrated polycyclic aromatic hydrocarbons

647   (niro-PAHs) (Bandowe and Meusel, 2017) or N-heterocyclic aromatics (Bandowe et al.,

648   2016) from combustion sources. The CHOS+ compounds have mostly unsaturated

649   hydrocarbons characteristics in representative U and S samples as discussed above but

650   were rarely detected in the R and site 120 samples. The CHONS+ did not show distinct

651   variations among investigated samples, but higher fraction of aliphatic/proteins-like

652   species in the S sample was observed.

653   As for ESI-, the O/C (mean: 0.41±0.02) and H/C (mean: 1.53±0.01) ratios were

654   highest for species identified in the S samples, reflecting their higher oxygenation and

655   saturation levels. These values are similar to those of soil water extracted organic matter

656   (Ohno et al., 2010). This future is consistent with the results of EEM-PARAFAC, which

657   showed that highly-oxygenated HULIS-1 dominates in S samples. Lignins/CRAMs-

658   like species detected in ESI- dominated the VK space rather than aliphatic/proteins-like

659   compounds detected in ESI+. The relative contributions of seven chemical classes did

660   not change much between U and R samples (Table 3). In S samples, lower fraction of

661   lignins/CRAMs-like species was found. Compared to the water extracted organic

662   matter from pure soil sample (Ohno et al., 2010), our S samples showed similar

Atmospheric
Chemistry
and Physics
Discussions
Open Access
EGU

663 percentage of lignins/CRAMs-like species (39% vs. 44%). An extremely high

664 contribution of lignins/CRAMs-like species (74.5%) was observed for the site 120

665 sample, strongly suggesting influence from biogenetic materials. As for the relative

666 abundances in major formula categories, CHO- and CHON- were dominated by

667 lignins/CRAMs-like species, except CHON- of the S sample, which exhibited highest

668 fraction of aliphatic/proteins-like species. This highest CHON- fraction mainly resulted

669 from a single compound with disproportionally high ion abundance, i.e., $C_9H_{17}O_3N$,

670 which might be tentatively assigned as amino acid and led to a high fraction of

671 aliphatic/proteins-like compounds in S samples (mean: 41%±1%). Amino acids are

672 widely distributed in soil and are important organic nitrogen sources of soil

673 microorganisms and plants (Geisseler et al., 2010). Moreover, biomass burning is also

674 a significant source of atmospheric amino acids (Laskin et al., 2009;Lin et al., 2012).

675 Therefore, either deposition of blowing soil or biomass burning aerosols may be

676 responsible for the appearance of this high-abundance amino acid species in the S

677 sample. As for CHOS- and CHONS-, lignins/CRAMs-like and carbohydrates-like

678 species accounted for large portions of their total intensity. Only a few CHONS-

679 compounds are apportioned as lignins/CRAMs-like species for the S sample, they are

680 attributed mostly to carbohydrates-like species than anything else. One interesting note

681 is that the contribution of condensed aromatics in the site 120 sample is highest among

682 all samples. Specifically, there are some unique CHONS- compounds within the region

683 of condensed aromatics, e.g., $C_{29}H_{14}O_4N_2S$ (DBE=24, AI=0.77) and $C_{26}H_{14}O_5N_2S$

684 (DBE=21, AI=0.72), which have high MW>400 Da. They may contain structure of

685 anthraquinones, which are widely distributed in nature plants (Duval et al., 2016).

686   To further illustrate the differences of chemical compositions and structures among

687 four groups of the investigated samples, plots of DBE versus C+N atomic number are

688 shown in Fig. 7. The numbers of unique formulas in the U sample were highest both in

689 ESI+ and ESI- with values of 578 and 618 (Fig. S8), respectively, which accounted for

690 44% and 54% of total assigned species in each of the modes. These values were lowest

691 for the R sample, with only 17% (145) and 11% (51) in ESI+ and ESI-, respectively.

692 These results reflect very high chemical complexity of WSOC from U samples. The

693 DBE plots of Fig. 7 are shown along with the reference lines depicting DBE values

694 characteristic of (a) linear polyenes (C_xH_{x+2}, DBE = 0.5 × C) (Cain et al., 2014); (b)

695 cata-condensed PAHs (DBE = 0.75 × C − 0.5) (Siegmann and Sattler, 2000); (c)

696 fullerene-like hydrocarbons (DBE = 0.9 × C) (Lobodin et al., 2012). Because efficient

697 absorption of visible light by organic molecules requires conjugated group of bonds

698 extended across a significant part of the molecule, the compounds with the *DBE/C*

699 greater than that of linear polyenes might be potential chromophores (Lin et al., 2018).

700 The DBE values of CHON and CHONS compounds shift 1−5 units to the right as the

701 sum-total number of carbon and nitrogen atoms are accounted for. In ESI-, 266 formulas

702 of the U sample were in the "BrC domain" region, which was much higher than the

703 other samples (26, 106, and 115 for the R, S, and site 120 sample, respectively). Most

704 of them are CHON-, CHOS- and CHONS- compounds, accounting for 74% of the total

705 formulas assigned in the U sample. Their C numbers and DBE values were mainly in

706 the ranges of 4-16 and 4-10, respectively. For the S and site 120 samples, CHO- and

707 CHON- were abundant in the "BrC domain" region (70% and 62% for the S and site

708 120 samples, respectively). The frequency distributions of C numbers and DBE were

709 similar between the U and S samples, but WSOC components in the S samples showed

710 higher *O/C* ratios for CHO- compounds (Fig. S9), again consistent with the soil organic

711 matter (Ohno et al., 2010). However, the observations are quite different for the site 120

712 sample, where C numbers and DBE values gathered in broader ranges of 11-26 and 10-

Atmospheric
Chemistry
and Physics
Discussions

Open Access

EGU

713   20, respectively, with higher medians. In addition, a few of the CHON- and CHONS-

714   compounds with DBE higher than 17 were detected. These CHONS- formulas have

715   been identified as plant-related organics as discussed above. Similarly, the highly

716   unsaturated CHON- compounds, e.g., $C_{25}H_{13}O_8N$ (DBE=20, AI=0.69), $C_{26}H_{15}O_8N$

717   (DBE=20, AI=0.65), and $C_{26}H_{15}O_9N$ (DBE=20, AI=0.63), showed high MW>400 Da,

718   and they may also be tentatively assigned as anthraquinone derivatives. All these unique

719   compounds suggested that the biogenic organics from plants are major sources of

720   WSOC from the site 120 sample. In ESI+, the numbers of formulas within "BrC domain"

721   were 216, 43, 103, and 64 for the U, R, S, and site 120 samples, respectively. These

722   potential BrC species were largely attributed to CHO+ and CHON+ compounds (54%-

723   75%), whereas the S-containing compounds (34%) were substantial in the U sample.

724   Although the U samples showed the highest number of unique "BrC" molecules,

725   their bulk *MAC* values are lower than those measured for the S and site 120 samples.

726   Observation of the lower *MAC* values in the U samples is consistent with HRMS

727   characterization results showing that the high-intensity WSOC compounds are out of

728   the "BrC domain" region as shown in Fig. 7.

729

730
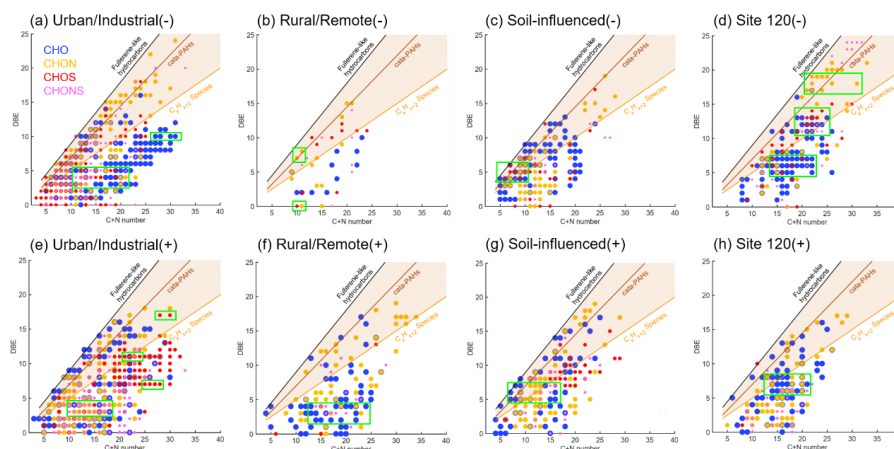
Figure 7. DBE vs. C+N number for unique molecules in representative samples from different groups. (a-d) ESI- and (e-h) ESI+. The reference lines indicate linear polyenes (C_xH_{x+2}, DBE = 0.5 × C), cata-condensed PAHs (DBE = 0.75 × C − 0.5), and fullerene-like hydrocarbons (DBE = 0.9 × C). Markers in the shaded area are potential BrC chromophores. The green boxes denote the high-intensity compounds. Four major formula categories are shown in different colors and sizes to avoid overlapping.

3.4 The radiative forcing by BrC attributed to WSOC in the snowpack

Inherent to the complexity of WSOC material and variability of its BrC optical properties, quantitative estimates of its *RF* in snowpack remain insufficiently studied. Yan et al. (2016) calculated the BrC-induced *RF* at LHG glacier from the TP region, which was 0.43 W m^{-2} and accounted for 10% of *RF* due to BC. Most recently, Beres et al. (2020) described the spectral albedo and *RF* after artificial deposition of BrC aerosol proxies from peat burning onto ambient snow surface. They showed that the instantaneous *RF* efficiency due to total deposited aerosol was 1.23 W m^{-2} per ppm of the deposited mass. However, in the real world, BrC concentrations may not be that high as in the proxy experiments. Also, daily averaged values of *RF* are more important for the climate research. Here we contribute to this line of work by calculating the

Atmospheric
Chemistry
and Physics
Discussions
Open Access
EGU

750   averaged-daily RF due to BC and BrC ($RF_{BC, BrC}$) deposits in snow based on the bulk

751   characterization measurements over the samples of our study.

752   Figure 8 shows the snow spectral albedo (α_λ) simulated for four different scenarios,

753   comparing albedo changes of the snowpack containing levels of BC and WSOC

754   measured in the samples. Because most of the snowpack was shallow during the

755   campaign, the albedo of pure snow was influenced by the effects of dark ground surface

756   (albedo assumed to be 0.2) underlaying at the snow depth specific to each of the sites,

757   as shown in Fig. 8. The average values of $\Delta\alpha$ and RF due to BC and BrC at different

758   spectral ranges are summarized in Table 4. As expected, BC have strong broadband

759   impact on the snow albedo and corresponding RF effects. Specifically, U and S samples

760   with high BC mass loadings (mean: 707 and 440 ng g^{-1}, respectively) show albedo

761   reduction ($\Delta\alpha_{BC}$) by 0.034 and 0.037 over broad 300-1500 nm wavelength range,

762   respectively, and the corresponding RF_{BC} estimates are as high as 3.5 W m^{-2}. In addition,

763   S and site 120 samples with higher WSOC concentrations (mean: 2082 and 7069 ng g^{-}

764   ^{1}, respectively) show lower broadband albedo reduction ($\Delta\alpha_{BrC}$) of ~0.006 and the

765   corresponding RF_{BrC} of ~0.6 W m^{-2}. Notably, because of the low BC and high WSOC

766   mass loadings in the site 120 sample, its RF_{BrC} estimate is approximately 2 times higher

767   than RF_{BC}. For the other samples (U, R, and S), the RF_{BrC} is still significant with the

768   average ratios of RF_{BrC}/RF_{BC} being at the level of 0.07-0.16. These results indicated that

769   BrC have profound impact on the reduction of the snow albedo in Northern Xinjiang.

770   As shown in Fig. 9, due to the stronger wavelength dependence of BrC absorption, the

771   spectral albedo reduction by BrC increased sharply at shorter wavelengths (300-400

772   nm), where $\Delta\alpha_{BrC}$ can be as large as 29-65% of the $\Delta\alpha_{BC}$ (Table 4). Unlike graphitic-like

773   components of BC, water-soluble part of BrC can trigger photochemical reactions in

774   snow forming reactive oxygen species (Fede and Grannas, 2015;Grannas et al., 2014),

Atmospheric
Chemistry
and Physics
Discussions

775   catalyzing reaction chemistry and accelerating its kinetics at snow/ice-air interface

776   (Grannas et al., 2014;Hullar et al., 2020). Overall, these results emphasize important

777   role of WSOC and its BrC components on tempering solar radiation balance and

778   modulating environmental chemistry of organics and their air-snow partitioning

779   pertinent to mid-latitude seasonal snowpack.

780

Atmospheric Chemistry and Physics Discussions — Open Access — EGU

781

782 **Table 4.** Simulated broadband albedo reduction due to BC and BrC within different wavelength ranges and the ratios between those of BrC and BC. The BC- and BrC-induced average-daily radiative forcing is also shown.

| | Broadband albedo reduction | | | | | | Radiative forcing | |
| | 300-400 nm | | | 300-1500 nm | | | BC ($W\ m^{-2}$) | BrC ($W\ m^{-2}$) |
	BC	BrC	BrC/BC	BC	BrC	BrC/BC		
U Industrial/Urban (n = 14)	0.059±0.056	0.015±0.013	0.29±0.19	0.034±0.034	0.002±0.002	0.07±0.06	3.38±3.54	0.21±0.21
R Remote/Rural (n = 10)	0.010±0.006	0.003±0.001	0.39±0.16	0.005±0.003	0.0004±0.0002	0.09±0.05	0.53±0.34	0.04±0.03
S Soil-influenced (n = 3)	0.069±0.001	0.044±0.025	0.65±0.37	0.037±0.002	0.006±0.003	0.16±0.08	3.49±0.26	0.55±0.28
Site 120 (n = 1)	0.005	0.066	12.02	0.003	0.006	2.16	0.27	0.59

783

784
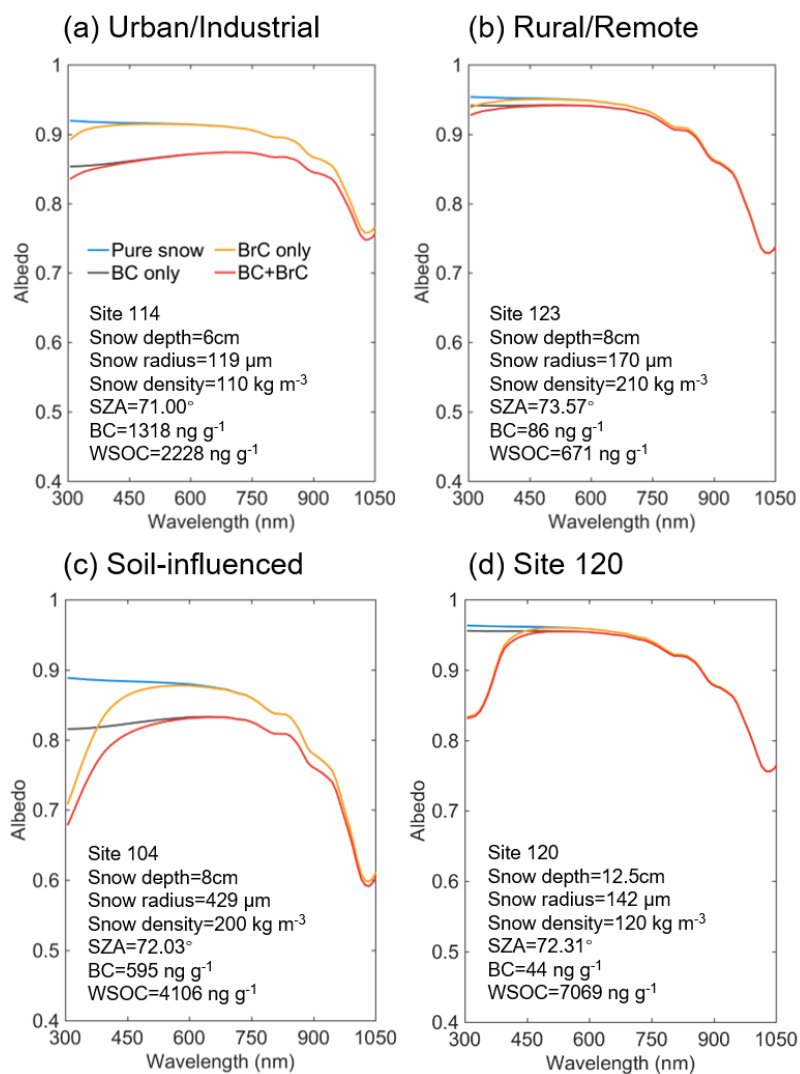
Figure 8. Simulated snow spectral albedo under different contamination scenarios for representative

samples from different groups. The blue, grey, yellow, and red lines exhibit the spectral albedos of

pure snow, BC- or BrC-contaminated snow, and snow polluted by both BC and BrC, respectively.

The input parameters of each site for SNICAR model are also shown.

789

(a) Urban/Industrial

(b) Rural/Remote

(c) Soil-influenced

(d) Site 120
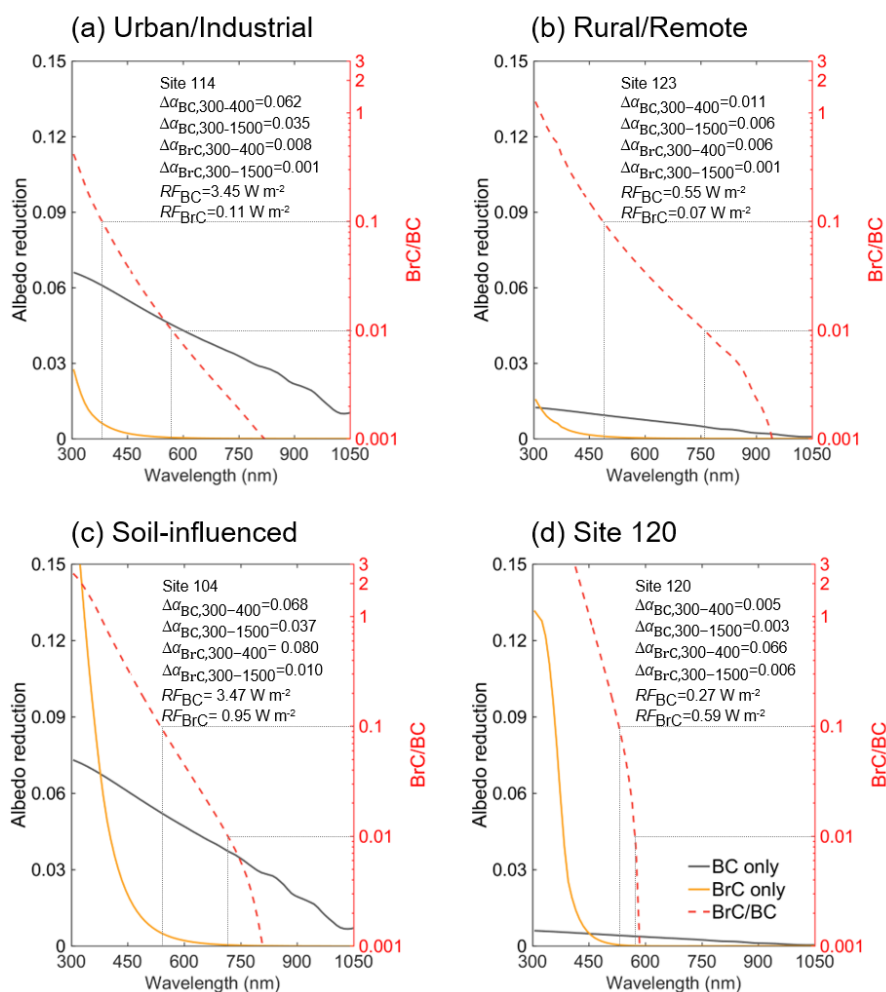
Figure 9. The albedo reduction spectra for representative samples from different groups. The grey and yellow lines show the albedo reductions due to BC or BrC, respectively. The red lines show the ratios of albedo reductions by BrC to those by BC. The $\Delta\alpha_{BC,BrC}$ and $RF_{BC,BrC}$ of each site are also shown.

4   Conclusions

The concentrations, optical properties, and molecular compositions of WSOC in seasonal snow collected from 28 sampling sites in Northern Xinjiang, northwestern China, were measured by multiple analytical techniques. The average concentrations of

Atmospheric
Chemistry
and Physics
Discussions

Open Access
EGU

800   WSOC were 1968±953 ng g^{-1}, 885±328 ng g^{-1}, 2082±1438 ng g^{-1}, and 7069 ng g^{-1} for

801   U, R, S, and site 120 samples, respectively, reflecting large variability of WSOC mass

802   loadings among different groups of sites. These values were generally higher than those

803   reported previously for samples from high-altitude or high-latitude regions. Site 120

804   sample showed the highest MAC_{365} (0.95 m^2 g^{-1}) along with an unusual shape of

805   absorption spectrum, followed by samples from S (0.94±0.31 m^2 g^{-1}), U (0.39±0.11 m^2

806   g^{-1}), and R (0.38±0.12 m^2 g^{-1}) sites. BrC components of our samples showed either

807   comparable or somewhat lower light-absorbing properties compared to previous reports

808   of polar or glacier snow, and were identified as W-BrC according to the optical-based

809   classification (Saleh, 2020).

810   The differences in bulk chemical composition among four groups of samples were

811   elucidated by EEM spectroscopy assisted with PARAFAC analysis. Terrestrial-sourced

812   HULIS-1 factor accounted for 49% of the total fluorescence in S samples, indicating

813   the significant contributions from soil organic material. HULIS-2 factor dominated the

814   fluorescence intensity of U samples (46%). The anthropogenic sources of HULIS-2

815   were inferred from significantly positive correlation with sulfate ions indicative

816   combustion related sources. PRLIS factor was abundant in R samples (48%), reflecting

817   a potential source of labile WSOC from microbial activities. The EEM map of site 120

818   showed a unique peak never found in any other samples, which might be from plant

819   organics.

820   HPLC-ESI-HRMS provided further information of molecular composition and

821   sources of WSOC. Total, 561 to 1487 and 339 to 1568 formulas were assigned in ESI+

822   and ESI- mass spectra, respectively. The mass distributions with respect to relative

823   intensity were highly variable among representative samples of different groups in both

824   ESI+ and ESI- modes, indicating different composition for each of the samples. CHO+

825 and CHON+ were the major components detected in ESI+ mode for all samples.

826 CHOS+ compounds were highly enriched in U samples. These species had low

827 oxidation degree, high unsaturation level and aromaticity, suggesting S-containing

828 aromatic organics presumably related to heavy fossil fuels. In the ESI- detection mode,

829 CHO- compounds were still dominated, but contribution from CHOS- was much higher,

830 showing roughly equal abundance with CHON-. Through analysis of the VK diagrams,

831 the major chemical species in snow WSOC were determined qualitatively. The

832 unsaturated hydrocarbons were the most abundant species in U samples, most of them

833 were CHOS+ from anthropogenic emissions. The R samples showed the highest

834 contribution from aliphatic/proteins-like species, which is consistent with the results

835 from EEM-PARAFAC analysis. The S samples showed high oxygenation and

836 saturation degrees, and indicated the similar values of O/C and H/C ratios and

837 percentage of lignins/CRAMs-like species compared to the soil organic matter (Ohno

838 et al., 2010). An extremely high contribution of lignins/CRAMs-like species were found

839 at the site 120 sample, suggesting the biogenetic sources of WSOC. Furthermore, a few

840 unique CHON- and CHONS- compounds with DBE higher than 17 and MW larger than

841 400 Da were found at site 120. The most possible candidates for them were species with

842 anthraquinone structures. Therefore, the special spectroscopic features of BrC from the

843 site 120 sample was attributed to biogenic organics from plants.

844   The RF due to BrC in snow was reported, for the first time, based on the field data

845 and model simulations. In general, the RF_{BrC} were at the levels of 0.04 to 0.59 W m^{-2}

846 among different groups of sites and contributed to 7% to 16% of RF_{BC}. Therefore, we

847 demonstrated the important influences of WSOC on the snow energy budget and

848 potentially on triggering snow photochemistry. This study presents a comprehensive

849 overview of WSOC and its BrC properties in seasonal snow of northwestern China,

850   which helps to better understand their characteristics, sources, and climate effects.

851

852   *Data availability.* Requests for all data in this study and any questions regarding the

853   data can be directed to Alexander Laskin (alaskin@purdue.edu) or Xin Wang

854   (wxin@lzu.edu.cn).

855

856   *Author contributions.* YZ, CW, AH, XN, and HW designed and conducted the lab

857   experiments. YZ processed the data with assist of CW and AH and wrote the paper. XW,

858   YZ, XN, JC, TS, WP, and HW designed and conducted the field campaign, collected

859   the snow samples, and discussed the results. AL and XW supervised this study. All co-

860   authors commented on the paper and improved it.

861

862   *Competing interests.* The authors declare that they have no conflict of interest.
863

871

References

Amoroso, A., Domine, F., Esposito, G., Morin, S., Savarino, J., Nardino, M., Montagnoli, M., Bonneville, J. M., Clement, J. C., Ianniello, A., and Beine, H. J.: Microorganisms in Dry Polar Snow Are Involved in the Exchanges of Reactive Nitrogen Species with the Atmosphere, Environ. Sci. Technol., 44, 714-719, 10.1021/es9027309, 2010.

Anastasio, C., and Robles, T.: Light absorption by soluble chemical species in Arctic and Antarctic snow, J. Geophys. Res. Atmos., 112, D24304, 10.1029/2007JD008695, 2007.

Andreae, M. O., and Gelencser, A.: Black carbon or brown carbon? The nature of light-absorbing carbonaceous aerosols, Atmos. Chem. Phys., 6, 3131-3148, 10.5194/acp-6-3131-2006, 2006.

Antony, R., Grannas, A. M., Willoughby, A. S., Sleighter, R. L., Thamban, M., and Hatcher, P. G.: Origin and Sources of Dissolved Organic Matter in Snow on the East Antarctic Ice Sheet, Environ. Sci. Technol., 48, 6151-6159, 10.1021/es405246a 2014.

Antony, R., Willoughby, A. S., Grannas, A. M., Catanzano, V., Sleighter, R. L., Thamban, M., Hatcher, P. G., and Nair, S.: Molecular Insights on Dissolved Organic Matter Transformation by Supraglacial Microbial Communities, Environ. Sci. Technol., 51, 4328-4337, 10.1021/acs.est.6b05780, 2017.

Bandowe, B. A., Meusel, H., Huang, R., Hoffmann, T., Cao, J., and Ho, K.: Azaarenes in fine particulate matter from the atmosphere of a Chinese megacity, Environ. Sci. Pollut. Res. Int., 23, 16025-16036, 10.1007/s11356-016-6740-z, 2016.

Bandowe, B. A. M., and Meusel, H.: Nitrated polycyclic aromatic hydrocarbons (nitro-PAHs) in the environment - A review, Sci. Total Environ., 581-582, 237-257, 10.1016/j.scitotenv.2016.12.115, 2017.

Bartels-Rausch, T., Brigante, M., Elshorbany, Y. F., Ammann, M., D'Anna, B., George, C., Stemmler, K., Ndour, M., and Kleffmann, J.: Humic acid in ice: Photo-enhanced conversion of nitrogen dioxide into nitrous acid, Atmos. Environ., 44, 5443-5450, 10.1016/j.atmosenv.2009.12.025, 2010.

Beine, H., Anastasio, C., Esposito, G., Patten, K., Wilkening, E., Domine, F., Voisin, D., Barret, M., Houdier, S., and Hall, S.: Soluble, light-absorbing species in snow at Barrow, Alaska, J. Geophys. Res. Atmos., 116, D00R05, 10.1029/2011jd016181, 2011.

Beres, N. D., Sengupta, D., Samburova, V., Khlystov, A. Y., and Moosmüller, H.: Deposition of brown carbon onto snow: changes in snow optical and radiative properties, Atmos. Chem. Phys., 20, 6095-6114, 10.5194/acp-20-6095-2020, 2020.

Bhatia, M. P., Das, S. B., Longnecker, K., Charette, M. A., and Kujawinski, E. B.: Molecular characterization of dissolved organic matter associated with the Greenland ice sheet, Geochim. Cosmochim. Acta, 74, 3768-3784, 10.1016/j.gca.2010.03.035, 2010.

Bianco, A., Deguillaume, L., Vaitilingom, M., Nicol, E., Baray, J. L., Chaumerliac, N., and Bridoux, M.: Molecular Characterization of Cloud Water Samples Collected at the Puy de Dome (France) by Fourier Transform Ion Cyclotron Resonance Mass Spectrometry, Environ. Sci. Technol., 52, 10275-10285, 10.1021/acs.est.8b01964, 2018.

Birdwell, J. E., and Valsaraj, K. T.: Characterization of dissolved organic matter in fogwater by excitation-emission matrix fluorescence spectroscopy, Atmos. Environ., 44, 3246-3253, 10.1016/j.atmosenv.2010.05.055, 2010.

Bond, T. C., and Bergstrom, R. W.: Light absorption by carbonaceous particles: An investigative review, Aerosol Sci. Technol., 40, 27-67, 10.1080/02786820500421521, 2006.

Bond, T. C., Doherty, S. J., Fahey, D. W., Forster, P. M., Berntsen, T., DeAngelo, B. J., Flanner, M. G., Ghan, S., Karcher, B., Koch, D., Kinne, S., Kondo, Y., Quinn, P. K., Sarofim, M. C., Schultz, M. G., Schulz, M., Venkataraman, C., Zhang, H., Zhang, S., Bellouin, N., Guttikunda, S. K., Hopke, P. K., Jacobson, M. Z., Kaiser, J. W., Klimont, Z., Lohmann, U., Schwarz, J. P., Shindell, D., Storelvmo, T., Warren, S. G., and Zender, C. S.: Bounding the role of black carbon in the climate system: A scientific assessment, J. Geophys. Res. Atmos., 118, 5380-5552, 10.1002/jgrd.50171, 2013.

Brutel-Vuilmet, C., Menegoz, M., and Krinner, G.: An analysis of present and future seasonal Northern Hemisphere land snow cover simulated by CMIP5 coupled climate models, Cryosphere, 7, 67-80, 10.5194/tc-7-67-2013, 2013.

Cain, J., Laskin, A., Kholghy, M. R., Thomson, M. J., and Wang, H.: Molecular characterization of organic content of soot along the centerline of a coflow diffusion flame, Phys. Chem. Chem. Phys., 16, 25862-25875, 10.1039/c4cp03330b, 2014.

Chen, Q., Mu, Z., Song, W., Wang, Y., Yang, Z., Zhang, L., and Zhang, Y. L.: Size-Resolved Characterization of the Chromophores in Atmospheric Particulate Matter From a Typical Coal-Burning City in China, J. Geophys. Res. Atmos., 124, 10546-10563, 10.1029/2019jd031149, 2019.

Chen, Q., Li, J., Hua, X., Jiang, X., Mu, Z., Wang, M., Wang, J., Shan, M., Yang, X., Fan, X., Song, J., Wang, Y., Guan, D., and Du, L.: Identification of species and sources of atmospheric chromophores by fluorescence excitation-emission matrix with parallel factor analysis, Sci. Total Environ., 718, 137322, 10.1016/j.scitotenv.2020.137322, 2020.

Chen, Q. C., Ikemori, F., and Mochida, M.: Light Absorption and Excitation-Emission Fluorescence of Urban Organic Aerosol Components and Their Relationship to Chemical Structure, Environ. Sci. Technol., 50, 10859-10868, 10.1021/acs.est.6b02541, 2016a.

Chen, Q. C., Miyazaki, Y., Kawamura, K., Matsumoto, K., Coburn, S., Volkamer, R., Iwamoto, Y., Kagami, S., Deng, Y. G., Ogawa, S., Ramasamy, S., Kato, S., Ida, A., Kajii, Y., and Mochida, M.: Characterization of Chromophoric Water-Soluble Organic Matter in Urban, Forest, and Marine Aerosols by HR-ToF-AMS Analysis and Excitation Emission Matrix Spectroscopy, Environ. Sci. Technol., 50, 10351-10360, 10.1021/acs.est.6b01643, 2016b.

Chen, Y., and Bond, T. C.: Light absorption by organic carbon from wood combustion, Atmos. Chem. Phys. , 10, 1773-1787, 10.5194/acp-10-1773-2010, 2010.

Coble, P. G.: Characterization of marine and terrestrial DOM in seawater using excitation emission matrix spectroscopy, Mar. Chem., 51, 325-346, Doi 10.1016/0304-4203(95)00062-3, 1996.

Coble, P. G., Del Castillo, C. E., and Avril, B.: Distribution and optical properties of CDOM in the Arabian Sea during the 1995 Southwest Monsoon, Deep-Sea Res. Pt. II, 45, 2195-2223, 10.1016/S0967-0645(98)00068-X, 1998.

Cook, J. M., Hodson, A. J., Gardner, A. S., Flanner, M., Tedstone, A. J., Williamson, C., Irvine-Fynn, T. D. L., Nilsson, J., Bryant, R., and Tranter, M.: Quantifying bioalbedo: a new physically based model and discussion of empirical methods for characterising biological influence on ice and snow albedo, Cryosphere, 11, 2611-2632, 10.5194/tc-11-2611-2017, 2017a.

972 Cook, J. M., Hodson, A. J., Taggart, A. J., Mernild, S. H., and Tranter, M.: A predictive
973   model for the spectral "bioalbedo" of snow, J. Geophys. Res. Earth, 122, 434-454,
974   10.1002/2016JF003932, 2017b.
975 DiDonato, N., Chen, H., Waggoner, D., and Hatcher, P. G.: Potential origin and
976   formation for molecular components of humic acids in soils, Geochim.
977   Cosmochim. Acta 178, 210-222, 10.1016/j.gca.2016.01.013, 2016.
978 Doherty, S. J., Warren, S. G., Grenfell, T. C., Clarke, A. D., and Brandt, R. E.: Light-
979   absorbing impurities in Arctic snow, Atmos. Chem. Phys., 10, 11647-11680,
980   10.5194/acp-10-11647-2010, 2010.
981 Duval, J., Pecher, V., Poujol, M., and Lesellier, E.: Research advances for the extraction,
982   analysis and uses of anthraquinones: A review, Ind. Crops Prod., 94, 812-833,
983   https://doi.org/10.1016/j.indcrop.2016.09.056, 2016.
984 Elliott, A., Mundy, C. J., Gosselin, M., Poulin, M., Campbell, K., and Wang, F.: Spring
985   production of mycosporine-like amino acids and other UV-absorbing compounds
986   in sea ice-associated algae communities in the Canadian Arctic, Mar. Ecol. Prog.
987   Ser., 541, 91-104, 10.3354/meps11540, 2015.
988 Fede, A., and Grannas, A. M.: Photochemical Production of Singlet Oxygen from
989   Dissolved Organic Matter in Ice, Environ. Sci. Technol., 49, 12808-12815,
990   10.1021/acs.est.5b03600, 2015.
991 Fellman, J. B., Hood, E., Raymond, P. A., Stubbins, A., and Spencer, R. G. M.: Spatial
992   Variation in the Origin of Dissolved Organic Carbon in Snow on the Juneau
993   Icefield, Southeast Alaska, Environ. Sci. Technol., 49, 11492-11499,
994   10.1021/acs.est.5b02685, 2015.
995 Feng, L., Xu, J. Z., Kang, S. C., Li, X. F., Li, Y., Jiang, B., and Shi, Q.: Chemical
996   Composition of Microbe-Derived Dissolved Organic Matter in Cryoconite in
997   Tibetan Plateau Glaciers: Insights from Fourier Transform Ion Cyclotron
998   Resonance Mass Spectrometry Analysis, Environ. Sci. Technol., 50, 13215-13223,
999   10.1021/acs.est.6b03971, 2016.
1000 Feng, L., An, Y., Xu, J., and Kang, S.: Characteristics and sources of dissolved organic
1001   matter in a glacier in the northern Tibetan Plateau: differences between different
1002   snow categories, Ann. Glaciol. , 59, 31-40, 10.1017/aog.2018.20, 2018.
1003 Feng, L., An, Y., Xu, J., Li, X., Jiang, B., and Liao, Y.: Biochemical evolution of
1004   dissolved organic matter during snow metamorphism across the ablation season
1005   for a glacier on the central Tibetan Plateau, Sci. Rep., 10, 6123, 10.1038/s41598-
1006   020-62851-w, 2020.
1007 Flanner, M. G., Zender, C. S., Randerson, J. T., and Rasch, P. J.: Present-day climate
1008   forcing and response from black carbon in snow, J. Geophys. Res. Atmos., 112,
1009   D11202, 10.1029/2006jd008003, 2007.
1010 Fu, P. Q., Kawamura, K., Chen, J., Qin, M. Y., Ren, L. J., Sun, Y. L., Wang, Z. F., Barrie,
1011   L. A., Tachibana, E., Ding, A. J., and Yamashita, Y.: Fluorescent water-soluble
1012   organic aerosols in the High Arctic atmosphere, Sci. Rep., 5, 9845,
1013   10.1038/Srep09845, 2015.
1014 Ganey, G. Q., Loso, M. G., Burgess, A. B., and Dial, R. J.: The role of microbes in
1015   snowmelt and radiative forcing on an Alaskan icefield, Nat. Geosci., 10, 754-759,
1016   10.1038/ngeo3027, 2017.
1017 Geisseler, D., Horwath, W. R., Joergensen, R. G., and Ludwig, B.: Pathways of nitrogen
1018   utilization by soil microorganisms – A review, Soil Biol. Biochem., 42, 2058-2067,
1019   10.1016/j.soilbio.2010.08.021, 2010.
1020 Grannas, A. M., Jones, A. E., Dibb, J., Ammann, M., Anastasio, C., Beine, H. J., Bergin,
1021   M., Bottenheim, J., Boxe, C. S., Carver, G., Chen, G., Crawford, J. H., Domine,

F., Frey, M. M., Guzman, M. I., Heard, D. E., Helmig, D., Hoffmann, M. R., Honrath, R. E., Huey, L. G., Hutterli, M., Jacobi, H. W., Klan, P., Lefer, B., McConnell, J., Plane, J., Sander, R., Savarino, J., Shepson, P. B., Simpson, W. R., Sodeau, J. R., von Glasow, R., Weller, R., Wolff, E. W., and Zhu, T.: An overview of snow photochemistry: evidence, mechanisms and impacts, Atmos. Chem. Phys., 7, 4329-4373, 10.5194/acp-7-4329-2007, 2007.

Grannas, A. M., Pagano, L. P., Pierce, B. C., Bobby, R., and Fede, A.: Role of dissolved organic matter in ice photochemistry, Environ. Sci. Technol., 48, 10725-10733, 10.1021/es5023834, 2014.

Hadley, O. L., and Kirchstetter, T. W.: Black-carbon reduction of snow albedo, Nat. Clim. Chang., 2, 437-440, 10.1038/Nclimate1433, 2012.

Hagler, G. S. W., Bergin, M. H., Smith, E. A., and Dibb, J. E.: A summer time series of particulate carbon in the air and snow at Summit, Greenland, J. Geophys. Res. Atmos., 112, D21309, 10.1029/2007jd008993, 2007a.

Hagler, G. S. W., Bergin, M. H., Smith, E. A., Dibb, J. E., Anderson, C., and Steig, E. J.: Particulate and water-soluble carbon measured in recent snow at Summit, Greenland, Geophys. Res. Lett., 34, 10.1029/2007GL030110, 2007b.

Hall, D. K., Riggs, G. A., and Salomonson, V. V.: Development of Methods for Mapping Global Snow Cover Using Moderate Resolution Imaging Spectroradiometer Data, Remote Sens. Environ., 54, 127-140, 10.1016/0034-4257(95)00137-P, 1995.

Hansen, J., and Nazarenko, L.: Soot climate forcing via snow and ice albedos, Proc. Nat. Acad. Sci. U.S.A., 101, 423-428, 10.1073/pnas.2237157100, 2004.

He, C. L., Li, Q. B., Liou, K. N., Takano, Y., Gu, Y., Qi, L., Mao, Y. H., and Leung, L. R.: Black carbon radiative forcing over the Tibetan Plateau, Geophys. Res. Lett., 41, 7806-7813, 10.1002/2014GL062191, 2014.

He, Z., Mao, J., Honeycutt, C. W., Ohno, T., Hunt, J. F., and Cade-Menun, B. J.: Characterization of plant-derived water extractable organic matter by multiple spectroscopic techniques, Biol. Fert. Soils, 45, 609-616, 10.1007/s00374-009-0369-8, 2009.

Hertkorn, N., Benner, R., Frommberger, M., Schmitt-Kopplin, P., Witt, M., Kaiser, K., Kettrup, A., and Hedges, J. I.: Characterization of a major refractory component of marine dissolved organic matter, Geochim. Cosmochim. Acta, 70, 2990-3010, 10.1016/j.gca.2006.03.021, 2006.

Hood, E., Battin, T. J., Fellman, J., O'Neel, S., and Spencer, R. G. M.: Storage and release of organic carbon from glaciers and ice sheets, Nat. Geosci., 8, 91-96, 10.1038/NGEO2331, 2015.

Huang, J. P., Fu, Q. A., Zhang, W., Wang, X., Zhang, R. D., Ye, H., and Warren, S. G.: Dust And Black Carbon In Seasonal Snow across Northern China, Bull. Am. Meteorol. Soc., 92, 175-181, 10.1175/2010BAMS3064.1, 2011.

Hullar, T., Bononi, F. C., Chen, Z., Magadia, D., Palmer, O., Tran, T., Rocca, D., Andreussi, O., Donadio, D., and Anastasio, C.: Photodecay of guaiacol is faster in ice, and even more rapid on ice, than in aqueous solution, Environ. Sci.-Proc. Imp., 22, 1666-1677, 10.1039/d0em00242a, 2020.

Hunt, J. F., and Ohno, T.: Characterization of Fresh and Decomposed Dissolved Organic Matter Using Excitation−Emission Matrix Fluorescence Spectroscopy and Multiway Analysis, J. Agric. Food. Chem., 55, 2121-2128, 10.1021/jf063336m, 2007.

Ikeya, K., Sleighter, R. L., Hatcher, P. G., and Watanabe, A.: Characterization of the chemical composition of soil humic acids using Fourier transform ion cyclotron resonance mass spectrometry, Geochim. Cosmochim. Acta, 153, 169-182,

1072   10.1016/j.gca.2015.01.002, 2015.
1073 Jacobson, M. Z.: Climate response of fossil fuel and biofuel soot, accounting for soot's
1074   feedback to snow and sea ice albedo and emissivity, J. Geophys. Res. Atmos., 109,
1075   D21201, 10.1029/2004jd004945, 2004.
1076 Jaffé, R., Cawley, K. M., and Yamashita, Y.: Applications of Excitation Emission Matrix
1077   Fluorescence with Parallel Factor Analysis (EEM-PARAFAC) in Assessing
1078   Environmental Dynamics of Natural Dissolved Organic Matter (DOM) in Aquatic
1079   Environments: A Review, in: Advances in the Physicochemical Characterization
1080   of Dissolved Organic Matter: Impact on Natural and Engineered Systems, ACS
1081   Symposium Series, 1160, American Chemical Society, 27-73, 2014.
1082 Jin, Z. H., Charlock, T. P., Rutledge, K., Stamnes, K., and Wang, Y. J.: Analytical
1083   solution of radiative transfer in the coupled atmosphere-ocean system with a rough
1084   surface, Appl. Opt., 45, 7443-7455, 10.1364/AO.45.007443, 2006.
1085 Jones, H. G.: The ecology of snow-covered systems: a brief overview of nutrient
1086   cycling   and   life   in   the   cold,   Hydrol.   Processes,   13,   2135-2147,
1087   10.1002/(SICI)1099-1085(199910)13:14/15<2135::AID-HYP862>3.0.CO;2-Y,
1088   1999.
1089 Kim, S., Kramer, R. W., and Hatcher, P. G.: Graphical method for analysis of ultrahigh-
1090   resolution broadband mass spectra of natural organic matter, the van Krevelen
1091   diagram, Anal. Chem., 75, 5336-5344, 10.1021/ac034415p, 2003.
1092 Kirchstetter, T. W., Novakov, T., and Hobbs, P. V.: Evidence that the spectral
1093   dependence of light absorption by aerosols is affected by organic carbon, J.
1094   Geophys. Res. Atmos., 109, D21208, 10.1029/2004jd004999, 2004.
1095 Kirillova, E. N., Andersson, A., Han, J., Lee, M., and Gustafsson, O.: Sources and light
1096   absorption of water-soluble organic carbon aerosols in the outflow from northern
1097   China, Atmos. Chem. Phys., 14, 1413-1422, 10.5194/acp-14-1413-2014, 2014.
1098 Koch, B. P., and Dittmar, T.: From mass to structure: an aromaticity index for high-
1099   resolution mass data of natural organic matter, Rapid Commun. Mass Spectrom.,
1100   20, 926-932, 10.1002/rcm.2386, 2006.
1101 Koch, B. P., and Dittmar, T.: From mass to structure: an aromaticity index for high-
1102   resolution mass data of natural organic matter, Rapid Commun. Mass Spectrom.,
1103   30, 250-250, 10.1002/rcm.7433, 2016.
1104 Kothawala, D. N., Murphy, K. R., Stedmon, C. A., Weyhenmeyer, G. A., and Tranvik,
1105   L. J.: Inner filter correction of dissolved organic matter fluorescence, Limnol.
1106   Oceanogr.-Meth., 11, 616-630, 10.4319/lom.2013.11.616, 2013.
1107 Laskin, A., Smith, J. S., Laskin, J. J. E. s., and technology: Molecular characterization
1108   of nitrogen-containing organic compounds in biomass burning aerosols using
1109   high-resolution mass spectrometry, Environ. Sci. Technol., 43, 3764-3771,
1110   10.1021/es803456n 2009.
1111 Laskin, A., Laskin, J., and Nizkorodov, S. A.: Chemistry of Atmospheric Brown Carbon,
1112   Chem. Rev., 115, 4335-4382, 10.1021/cr5006167, 2015.
1113 Lawaetz, A. J., and Stedmon, C. A.: Fluorescence Intensity Calibration Using the
1114   Raman   Scatter   Peak   of   Water,   Appl.   Spectrosc.,   63,   936-940,
1115   10.1366/000370209788964548, 2009.
1116 Legrand, M., Preunkert, S., Jourdain, B., Guilhermet, J., Fain, X., Alekhina, I., and Petit,
1117   J. R.: Water-soluble organic carbon in snow and ice deposited at Alpine, Greenland,
1118   and Antarctic sites: a critical review of available data and their atmospheric
1119   relevance, Clim. Past, 9, 2195-2211, 10.5194/cp-9-2195-2013, 2013.
1120 Lin, P., Engling, G., and Yu, J. Z.: Humic-like substances in fresh emissions of rice
1121   straw burning and in ambient aerosols in the Pearl River Delta Region, China,

1122   Atmos. Chem. Phys., 10, 6487-6500, 10.5194/acp-10-6487-2010, 2010.

1123 Lin, P., Rincon, A. G., Kalberer, M., and Yu, J. Z.: Elemental composition of HULIS in
1124   the Pearl River Delta Region, China: results inferred from positive and negative
1125   electrospray high resolution mass spectrometric data, Environ. Sci. Technol., 46,
1126   7454-7462, 10.1021/es300285d, 2012.

1127 Lin, P., Aiona, P. K., Li, Y., Shiraiwa, M., Laskin, J., Nizkorodov, S. A., and Laskin, A.:
1128   Molecular Characterization of Brown Carbon in Biomass Burning Aerosol
1129   Particles, Environ. Sci. Technol., 50, 11815-11824, 10.1021/acs.est.6b03024, 2016.

1130 Lin, P., Fleming, L. T., Nizkorodov, S. A., Laskin, J., and Laskin, A.: Comprehensive
1131   Molecular Characterization of Atmospheric Brown Carbon by High Resolution
1132   Mass Spectrometry with Electrospray and Atmospheric Pressure Photoionization,
1133   Anal. Chem., 90, 12493-12502, 10.1021/acs.analchem.8b02177, 2018.

1134 Liu, Y. Q., Yao, T. D., Jiao, N. Z., Kang, S. C., Xu, B. Q., Zeng, Y. H., Huang, S. J., and
1135   Liu, X. B.: Bacterial diversity in the snow over Tibetan Plateau Glaciers,
1136   Extremophiles, 13, 411-423, 10.1007/s00792-009-0227-5, 2009.

1137 Lobodin, V. V., Marshall, A. G., and Hsu, C. S.: Compositional Space Boundaries for
1138   Organic Compounds, Anal. Chem., 84, 3410-3416, 10.1021/ac300244f, 2012.

1139 Lu, Y., Li, X., Mesfioui, R., Bauer, J. E., Chambers, R. M., Canuel, E. A., and Hatcher,
1140   P. G.: Use of ESI-FTICR-MS to Characterize Dissolved Organic Matter in
1141   Headwater Streams Draining Forest-Dominated and Pasture-Dominated
1142   Watersheds, Plos One, 10, e0145639, 10.1371/journal.pone.0145639, 2015a.

1143 Lu, Z., Streets, D. G., Winijkul, E., Yan, F., Chen, Y., Bond, T. C., Feng, Y., Dubey, M.
1144   K., Liu, S., Pinto, J. P., and Carmichael, G. R.: Light absorption properties and
1145   radiative effects of primary organic aerosol emissions, Environ. Sci. Technol., 49,
1146   4868-4877, 10.1021/acs.est.5b00211, 2015b.

1147 Lutz, S., Anesio, A. M., Villar, S. E. J., and Benning, L. G.: Variations of algal
1148   communities cause darkening of a Greenland glacier, FEMS Microbiol. Ecol., 89,
1149   402-414, 10.1111/1574-6941.12351, 2014.

1150 McLafferty, F. W., Tureček, F., and Turecek, F.: Interpretation of mass spectra,
1151   University science books, 1993.

1152 McNeill, V. F., Grannas, A. M., Abbatt, J. P. D., Ammann, M., Ariya, P., Bartels-Rausch,
1153   T., Domine, F., Donaldson, D. J., Guzman, M. I., Heger, D., Kahan, T. F., Klan, P.,
1154   Masclin, S., Toubin, C., and Voisin, D.: Organics in environmental ices: sources,
1155   chemistry, and impacts, Atmos. Chem. Phys., 12, 9653-9678, 10.5194/acp-12-
1156   9653-2012, 2012.

1157 Mead, R. N., Felix, J. D., Avery, G. B., Kieber, R. J., Willey, J. D., and Podgorski, D.
1158   C.: Characterization of CHOS compounds in rainwater from continental and
1159   coastal storms by ultrahigh resolution mass spectrometry, Atmos. Environ., 105,
1160   162-168, 10.1016/j.atmosenv.2015.01.057, 2015.

1161 Mladenov, N., Alados-Arboledas, L., Olmo, F. J., Lyamani, H., Delgado, A., Molina,
1162   A., and Reche, I.: Applications of optical spectroscopy and stable isotope analyses
1163   to organic aerosol source discrimination in an urban area, Atmos. Environ., 45,
1164   1960-1969, 10.1016/j.atmosenv.2011.01.029, 2011.

1165 Mladenov, N., Williams, M. W., Schmidt, S. K., and Cawley, K.: Atmospheric
1166   deposition as a source of carbon and nutrients to an alpine catchment of the
1167   Colorado Rocky Mountains, Biogeosciences, 9, 3337-3355, 10.5194/bg-9-3337-
1168   2012, 2012.

1169 Murphy, K. R., Stedmon, C. A., Waite, T. D., and Ruiz, G. M.: Distinguishing between
1170   terrestrial and autochthonous organic matter sources in marine environments using
1171   fluorescence spectroscopy, Mar. Chem., 108, 40-58,

1172   10.1016/j.marchem.2007.10.003, 2008.
1173   Murphy, K. R., Stedmon, C. A., Graeber, D., and Bro, R.: Fluorescence spectroscopy
1174   and multi-way techniques. PARAFAC, Anal. Methods, 5, 6557-6566,
1175   10.1039/c3ay41160e, 2013.
1176   Myers, O. D., Sumner, S. J., Li, S., Barnes, S., and Du, X.: One Step Forward for
1177   Reducing False Positive and False Negative Compound Identifications from Mass
1178   Spectrometry Metabolomics Data: New Algorithms for Constructing Extracted
1179   Ion Chromatograms and Detecting Chromatographic Peaks, Anal. Chem., 89,
1180   8696-8703, 10.1021/acs.analchem.7b00947, 2017.
1181   Ning, C., Gao, Y., Zhang, H., Yu, H., Wang, L., Geng, N., Cao, R., and Chen, J.:
1182   Molecular characterization of dissolved organic matters in winter atmospheric fine
1183   particulate matters (PM2.5) from a coastal city of northeast China, Sci. Total
1184   Environ., 689, 312-321, 10.1016/j.scitotenv.2019.06.418, 2019.
1185   Niu, H. W., Kang, S. C., Lu, X. X., and Shi, X. F.: Distributions and light absorption
1186   property of water soluble organic carbon in a typical temperate glacier,
1187   southeastern Tibetan Plateau, Tellus B, 70, 10.1080/16000889.2018.1468705,
1188   2018.
1189   Nizkorodov, S. A., Laskin, J., and Laskin, A.: Molecular chemistry of organic aerosols
1190   through the application of high resolution mass spectrometry, Phys. Chem. Chem.
1191   Phys., 13, 3612-3629, 10.1039/c0cp02032j, 2011.
1192   Noziere, B., Kalberer, M., Claeys, M., Allan, J., D'Anna, B., Decesari, S., Finessi, E.,
1193   Glasius, M., Grgic, I., Hamilton, J. F., Hoffmann, T., Iinuma, Y., Jaoui, M., Kahnt,
1194   A., Kampf, C. J., Kourtchev, I., Maenhaut, W., Marsden, N., Saarikoski, S.,
1195   Schnelle-Kreis, J., Surratt, J. D., Szidat, S., Szmigielski, R., and Wisthaler, A.: The
1196   molecular identification of organic compounds in the atmosphere: state of the art
1197   and challenges, Chem. Rev., 115, 3919-3983, 10.1021/cr5003485, 2015.
1198   Ohno, T., He, Z., Sleighter, R. L., Honeycutt, C. W., and Hatcher, P. G.: Ultrahigh
1199   resolution mass spectrometry and indicator species analysis to identify marker
1200   components of soil- and plant biomass- derived organic matter fractions, Environ.
1201   Sci. Technol., 44, 8594-8600, 10.1021/es101089t, 2010.
1202   Painter, T. H., Deems, J. S., Belnap, J., Hamlet, A. F., Landry, C. C., and Udall, B.:
1203   Response of Colorado River runoff to dust radiative forcing in snow, Proc. Nat.
1204   Acad. Sci. U.S.A., 107, 17125-17130, 10.1073/pnas.0913139107, 2010.
1205   Painter, T. H., Seidel, F. C., Bryant, A. C., McKenzie Skiles, S., and Rittger, K.: Imaging
1206   spectroscopy of albedo and radiative forcing by light-absorbing impurities in
1207   mountain snow, J. Geophys. Res. Atmos., 118, 9511-9523, 10.1002/jgrd.50520,
1208   2013.
1209   Pluskal, T., Castillo, S., Villar-Briones, A., and Orešič, M.: MZmine 2: modular
1210   framework for processing, visualizing, and analyzing mass spectrometry-based
1211   molecular profile data, BMC Bioinf., 11, 395, 10.1186/1471-2105-11-395, 2010.
1212   Pöhlker, C., Huffman, J. A., and Pöschl, U.: Autofluorescence of atmospheric
1213   bioaerosols – fluorescent biomolecules and potential interferences, Atmos. Meas.
1214   Tech., 5, 37-71, 10.5194/amt-5-37-2012, 2012.
1215   Pu, W., Wang, X., Wei, H. L., Zhou, Y., Shi, J. S., Hu, Z. Y., Jin, H. C., and Chen, Q. L.:
1216   Properties of black carbon and other insoluble light-absorbing particles in seasonal
1217   snow of northwestern China, Cryosphere, 11, 1213-1233, 10.5194/tc-11-1213-
1218   2017, 2017.
1219   Pu, W., Cui, J., Shi, T., Zhang, X., He, C., and Wang, X.: The remote sensing of radiative
1220   forcing by light-absorbing particles (LAPs) in seasonal snow over northeastern
1221   China, Atmos. Chem. Phys. , 19, 9949-9968, 10.5194/acp-19-9949-2019, 2019.

Qi, Y., Fu, P., and Volmer, D. A.: Analysis of natural organic matter via fourier transform ion cyclotron resonance mass spectrometry: an overview of recent non-petroleum applications, Mass Spectrom. Rev., 10.1002/mas.21634, 2020.

Qian, Y., Wang, H., Zhang, R., Flanner, M. G., and Rasch, P. J.: A sensitivity study on modeling black carbon in snow and its radiative forcing over the Arctic and Northern China, Environ. Res. Lett. , 9, 10.1088/1748-9326/9/6/064001, 2014.

Roach, P. J., Laskin, J., and Laskin, A.: Higher-order mass defect analysis for mass spectra of complex organic mixtures, Anal. Chem., 83, 4924-4929, 10.1021/ac200654j, 2011.

Saleh, R.: From Measurements to Models: Toward Accurate Representation of Brown Carbon in Climate Calculations, Curr. Pollut. Rep., 6, 90-104, 10.1007/s40726-020-00139-3, 2020.

Seinfeld, J. H., and Pandis, S. N.: Atmospheric chemistry and physics: from air pollution to climate change, 3rd ed., John Wiley & Sons, 2016.

Shi, T., Pu, W., Zhou, Y., Cui, J., Zhang, D., and Wang, X.: Albedo of Black Carbon-Contaminated Snow Across Northwestern China and the Validation With Model Simulation, J. Geophys. Res. Atmos., 125, 10.1029/2019jd032065, 2020.

Shick, J. M., and Dunlap, W. C.: Mycosporine-like amino acids and related Gadusols: biosynthesis, acumulation, and UV-protective functions in aquatic organisms, Annu. Rev. Physiol., 64, 223-262, 10.1146/annurev.physiol.64.081501.155802, 2002.

Siegmann, K., and Sattler, K.: Formation mechanism for polycyclic aromatic hydrocarbons in methane flames, J. Chem. Phys., 112, 698-709, 10.1063/1.480648, 2000.

Singer, G. A., Fasching, C., Wilhelm, L., Niggemann, J., Steier, P., Dittmar, T., and Battin, T. J.: Biogeochemically diverse organic matter in Alpine glaciers and its downstream fate, Nat. Geosci., 5, 710-714, 10.1038/NGEO1581, 2012.

Skiles, S. M., Flanner, M., Cook, J. M., Dumont, M., and Painter, T. H.: Radiative forcing by light-absorbing particles in snow, Nat. Clim. Chang., 8, 964-971, 10.1038/s41558-018-0296-5, 2018.

Spencer, R. G. M., Guo, W. D., Raymond, P. A., Dittmar, T., Hood, E., Fellman, J., and Stubbins, A.: Source and biolability of ancient dissolved organic matter in glacier and lake ecosystems on the Tibetan Plateau, Geochim. Cosmochim. Acta, 142, 64-74, 10.1016/j.gca.2014.08.006, 2014.

Stedmon, C. A., Markager, S., and Bro, R.: Tracing dissolved organic matter in aquatic environments using a new approach to fluorescence spectroscopy, Mar. Chem., 82, 239-254, 10.1016/S0304-4203(03)00072-0, 2003.

Stedmon, C. A., and Markager, S.: Resolving the variability in dissolved organic matter fluorescence in a temperate estuary and its catchment using PARAFAC analysis, Limnol. Oceanogr., 50, 686-697, 10.4319/lo.2005.50.2.0686, 2005.

Stedmon, C. A., and Bro, R.: Characterizing dissolved organic matter fluorescence with parallel factor analysis: a tutorial, Limnol. Oceanogr.-Meth., 6, 572-579, 10.4319/lom.2008.6.572, 2008.

Sun, H. L., Biedermann, L., and Bond, T. C.: Color of brown carbon: A model for ultraviolet and visible light absorption by organic carbon aerosol, Geophys. Res. Lett. , 34, L17813, 10.1029/2007gl029797, 2007.

Toon, O. B., Mckay, C. P., Ackerman, T. P., and Santhanam, K.: Rapid Calculation of Radiative Heating Rates and Photodissociation Rates in Inhomogeneous Multiple-Scattering Atmospheres, J. Geophys. Res. Atmos., 94, 16287-16301, 10.1029/JD094iD13p16287, 1989.

1272   Voisin, D., Jaffrezo, J. L., Houdier, S., Barret, M., Cozic, J., King, M. D., France, J. L.,
1273   Reay, H. J., Grannas, A., Kos, G., Ariya, P. A., Beine, H. J., and Domine, F.:
1274   Carbonaceous species and humic like substances (HULIS) in Arctic snowpack
1275   during OASIS field campaign in Barrow, J. Geophys. Res. Atmos., 117, D00r19,
1276   10.1029/2011jd016612, 2012.
1277   Wang, K., Zhang, Y., Huang, R.-J., Cao, J., and Hoffmann, T.: UHPLC-Orbitrap mass
1278   spectrometric characterization of organic aerosol from a central European city
1279   (Mainz, Germany) and a Chinese megacity (Beijing), Atmos. Environ., 189, 22-
1280   29, 10.1016/j.atmosenv.2018.06.036, 2018.
1281   Wang, X., Doherty, S. J., and Huang, J.: Black carbon and other light-absorbing
1282   impurities in snow across Northern China, J. Geophys. Res. Atmos., 118, 1471-
1283   1492, 10.1029/2012JD018291, 2013.
1284   Wang, X., Hayeck, N., Brüggemann, M., Yao, L., Chen, H., Zhang, C., Emmelin, C.,
1285   Chen, J., George, C., and Wang, L.: Chemical Characteristics of Organic Aerosols
1286   in Shanghai: A Study by Ultrahigh-Performance Liquid Chromatography Coupled
1287   With Orbitrap Mass Spectrometry, J. Geophys. Res. Atmos., 122, 11,703-711,722,
1288   10.1002/2017jd026930, 2017a.
1289   Wang, X., Pu, W., Ren, Y., Zhang, X., Zhang, X., Shi, J., Jin, H., Dai, M., and Chen, Q.:
1290   Observations and model simulations of snow albedo reduction in seasonal snow
1291   due to insoluble light-absorbing particles during 2014 Chinese survey, Atmos.
1292   Chem. Phys., 17, 2279-2296, 10.5194/acp-17-2279-2017, 2017b.
1293   Wang, X., Hayeck, N., Brüggemann, M., Abis, L., Riva, M., Lu, Y., Wang, B., Chen, J.,
1294   George, C., and Wang, L.: Chemical characteristics and brown carbon
1295   chromophores of atmospheric organic aerosols over the Yangtze River channel: a
1296   cruise campaign, J. Geophys. Res. Atmos., 10.1029/2020jd032497, 2020a.
1297   Wang, X., Zhang, X., and Di, W.: Development of an improved two-sphere integration
1298   technique for quantifying black carbon concentrations in the atmosphere and
1299   seasonal snow, Atmos. Meas. Tech., 13, 39-52, 10.5194/amt-13-39-2020, 2020b.
1300   Wiscombe, W. J., and Warren, S. G.: A Model for the Spectral Albedo of Snow .1. Pure
1301   Snow,   J.   Atmos.   Sci.,   37,   2712-2733,   10.1175/1520-
1302   0469(1980)037<2712:AMFTSA>2.0.CO;2, 1980.
1303   Wu, C., Yang, J., Fu, Q., Zhu, B., Ruan, T., and Jiang, G.: Molecular characterization
1304   of water-soluble organic compounds in PM2.5 using ultrahigh resolution mass
1305   spectrometry, Sci. Total Environ. , 668, 917-924, 10.1016/j.scitotenv.2019.03.031,
1306   2019a.
1307   Wu, G., Ram, K., Fu, P., Wang, W., Zhang, Y., Liu, X., Stone, E. A., Pradhan, B. B.,
1308   Dangol, P. M., Panday, A. K., Wan, X., Bai, Z., Kang, S., Zhang, Q., and Cong, Z.:
1309   Water-Soluble Brown Carbon in Atmospheric Aerosols from Godavari (Nepal), a
1310   Regional Representative of South Asia, Environ. Sci. Technol., 53, 3471-3479,
1311   10.1021/acs.est.9b00596, 2019b.
1312   Wu, G., Wan, X., Ram, K., Li, P., Liu, B., Yin, Y., Fu, P., Loewen, M., Gao, S., Kang,
1313   S., Kawamura, K., Wang, Y., and Cong, Z.: Light absorption, fluorescence
1314   properties and sources of brown carbon aerosols in the Southeast Tibetan Plateau,
1315   Environ. Pollut., 257, 113616, 10.1016/j.envpol.2019.113616, 2020.
1316   Wu, G., Fu, P., Ram, K., Song, J., Chen, Q., Kawamura, K., Wan, X., Kang, S., Wang,
1317   X., Laskin, A., and Cong, Z.: Fluorescence characteristics of water-soluble organic
1318   carbon   in   atmospheric   aerosol,   Environ.   Pollut.,   268,   115906,
1319   https://doi.org/10.1016/j.envpol.2020.115906, 2021.
1320   Xie, Q., Su, S., Chen, S., Zhang, Q., Yue, S., Zhao, W., Du, H., Ren, H., Wei, L., dong,
1321   c., Xu, Y.-s., Sun, Y., Wang, Z., and Fu, P.: Molecular Characterization of Size-

Segregated Organic Aerosols in the Urban Boundary Layer in Wintertime Beijing by FT-ICR MS, Faraday Discuss., 10.1039/d0fd00084a, 2020.

Xu, C., Chen, Y., Yang, Y., Hao, X., and Shen, Y.: Hydrology and water resources variation and its response to regional climate change in Xinjiang, J. Geog. Sci., 20, 599-612, 10.1007/s11442-010-0599-6, 2010.

Yan, F. P., Kang, S. C., Li, C. L., Zhang, Y. L., Qin, X., Li, Y., Zhang, X. P., Hu, Z. F., Chen, P. F., Li, X. F., Qu, B., and Sillanpaa, M.: Concentration, sources and light absorption characteristics of dissolved organic carbon on a medium-sized valley glacier, northern Tibetan Plateau, Cryosphere, 10, 2611-2621, 10.5194/tc-10-2611-2016, 2016.

Ye, H., Zhang, R. D., Shi, J. S., Huang, J. P., Warren, S. G., and Fu, Q.: Black carbon in seasonal snow across northern Xinjiang in northwestern China, Environ. Res. Lett., 7, 044002, 10.1088/1748-9326/7/4/044002, 2012.

Zatko, M. C., Grenfell, T. C., Alexander, B., Doherty, S. J., Thomas, J. L., and Yang, X.: The influence of snow grain size and impurities on the vertical profiles of actinic flux and associated NOx emissions on the Antarctic and Greenland ice sheets, Atmos. Chem. Phys., 13, 3547-3567, 2013.

Zhang, Y., Kang, S., Gao, T., Schmale, J., Liu, Y., Zhang, W., Guo, J., Du, W., Hu, Z., Cui, X., and Sillanpaa, M.: Dissolved organic carbon in snow cover of the Chinese Altai Mountains, Central Asia: Concentrations, sources and light-absorption properties, Sci. Total Environ., 647, 1385-1397, 10.1016/j.scitotenv.2018.07.417, 2019.

Zhang, Y., Kang, S., Gao, T., Sprenger, M., Dou, T., Han, W., Zhang, Q., Sun, S., Du, W., Chen, P., Guo, J., Cui, X., and Sillanpää, M.: Dissolved organic carbon in Alaskan Arctic snow: concentrations, light-absorption properties, and bioavailability, Tellus B, 72, 1-19, 10.1080/16000889.2020.1778968, 2020.

Zhang, Y. L., Zhang, E. L., Yin, Y., van Dijk, M. A., Feng, L. Q., Shi, Z. Q., Liu, M. L., and Qin, B. Q.: Characteristics and sources of chromophoric dissolved organic matter in lakes of the Yungui Plateau, China, differing in trophic state and altitude, Limnol. Oceanogr., 55, 2645-2659, 10.4319/lo.2010.55.6.2645, 2010.

Zhang, Y. L., El-Haddad, I., Huang, R. J., Ho, K. F., Cao, J. J., Han, Y. M., Zotter, P., Bozzetti, C., Daellenbach, K. R., Slowik, J. G., Salazar, G., Prevot, A. S. H., and Szidat, S.: Large contribution of fossil fuel derived secondary organic carbon to water soluble organic aerosols in winter haze in China, Atmos. Chem. Phys., 18, 4005-4017, 10.5194/acp-18-4005-2018, 2018a.

Zhang, Y. L., Kang, S. C., Sprenger, M., Cong, Z. Y., Gao, T. G., Li, C. L., Tao, S., Li, X. F., Zhong, X. Y., Xu, M., Meng, W. J., Neupane, B., Qin, X., and Sillanpaa, M.: Black carbon and mineral dust in snow cover on the Tibetan Plateau, Cryosphere, 12, 413-431, 10.5194/tc-12-413-2018, 2018b.

Zhao, C., Hu, Z., Qian, Y., Leung, L. R., Huang, J., Huang, M., Jin, J., Flanner, M. G., Zhang, R., Wang, H., Yan, H., Lu, Z., and Streets, D. G.: Simulating black carbon and dust and their radiative forcing in seasonal snow: a case study over North China with field campaign measurements, Atmos. Chem. Phys., 14, 11475-11491, 10.5194/acp-14-11475-2014, 2014.

Zhao, Y., Song, K., Wen, Z., Li, L., Zang, S., Shao, T., Li, S., and Du, J.: Seasonal characterization of CDOM for lakes in semiarid regions of Northeast China using excitation–emission matrix fluorescence and parallel factor analysis (EEM–PARAFAC), Biogeosciences, 13, 1635-1645, 10.5194/bg-13-1635-2016, 2016.

Zhou, L., Zhou, Y., Hu, Y., Cai, J., Liu, X., Bai, C., Tang, X., Zhang, Y., Jang, K. S., Spencer, R. G. M., and Jeppesen, E.: Microbial production and consumption of

1372   dissolved organic matter in glacial ecosystems on the Tibetan Plateau, Water Res.,
1373   160, 18-28, 10.1016/j.watres.2019.05.048, 2019a.
1374 Zhou, Y., Wen, H., Liu, J., Pu, W., Chen, Q., and Wang, X.: The optical characteristics
1375   and sources of chromophoric dissolved organic matter (CDOM) in seasonal snow
1376   of northwestern China, Cryosphere, 13, 157-175, 10.5194/tc-13-157-2019, 2019b.
1377 Zhou, Y., Zhou, L., He, X., Jang, K. S., Yao, X., Hu, Y., Zhang, Y., Li, X., Spencer, R.
1378   G. M., Brookes, J. D., and Jeppesen, E.: Variability in Dissolved Organic Matter
1379   Composition and Biolability across Gradients of Glacial Coverage and Distance
1380   from Glacial Terminus on the Tibetan Plateau, Environ. Sci. Technol., 53, 12207-
1381   12217, 10.1021/acs.est.9b03348, 2019c.